MAPPING WEAK GRAVITATIONAL LENSING SIGNALS
FROM LOW-REDSHIFT GALAXY CLUSTERS
TO COMPARE DARK MATTER AND X-RAY GAS SUBSTRUCTURES.

CLAIRE HAWKINS

BROWN UNIVERSITY

MAY 2020

Contents

Acknowledgements:

I want to thank Professor Ian Dell'Antonio for his mentorship and the time he has spent working with me throughout this process. He's been a dedicated teacher, a caring academic advisor, and an invested thesis advisor. My growth as a physics student and astro-enthusiast is due in large part to his courses and my experience in his lab. Even after the transition to online classes, his course has remained a highlight of the semester. I really appreciate the thought he has put into maintaining our dispersed community and how accessible he continues to be.

I also want to give a big thanks to Shenming Fu for all of his help in the lab. His manual for the LSST obs_decam pipeline was indispensable to my project. I am grateful for his willingness to answer all of my questions, as simple or as time-consuming as they were. Also, thanks to Natalie and Lexi for working with me this summer, I'm so glad to have been on your team. And thanks Andrea and Nick for everything this semester, I really enjoyed seeing your theses come together.

Finally, I want to thank Professor Dave Cutts for pulling me into the world of astrophysics at Brown. Working with him on the introductory astronomy course has helped me understand how deeply I love teaching and sharing the night sky with others.

Abstract:

Galaxy clusters are the largest gravitationally bound systems in our universe and roughly 85% of their mass is contributed by dark matter. The rest of their mass is dominated by the baryonic constituents of hot X-ray emitting gas and luminous galaxies. In this project, I compared the density distribution of dark matter and X-ray emitting gas in nearby galaxy clusters. These comparisons can shed light on the evolutionary status of the cluster. I mapped the distribution of X-ray emitting gas directly from Chandra X-ray observations. However, because dark matter doesn't directly interact with photons, it has to be detected indirectly. The presence of mass within Galaxy clusters distorts the images of elliptical galaxies behind the cluster, in an effect called gravitational lensing. The majority of lensing from clusters is in the form of weak gravitational lensing (WL), which is detected as a statistical tangential shear pattern of the background galaxies and is used to build 2-dimensional mass maps of the cluster. The vast majority of cluster mass is in the form of dark matter, so we approximate the mass distribution as that of the dark matter. By examining X-ray and dark matter morphology, we can learn about the recent mergers in clusters and their evolutionary formation histories.

Introduction:

Gravity binds massive objects throughout the universe. Galaxies are gravitationally bound systems of gas, dust, and millions, if not billions, of stars. Many of these galaxies are, themselves, members of the largest gravitationally bound structures in the universe: galaxy clusters. The familiar components of these clusters: the stars, dust, and gas (the baryonic components) have been shown in X-ray studies to constitute only a small portion of the overall clusters' mass (roughly 10-15%). Dark matter, which can't be seen directly and whose presence must, therefore, be inferred indirectly, accounts for the remaining mass.

Gravitational lensing is our best way of indirectly measuring dark matter. During the 1919 solar eclipse, Sir Arthur Eddington detected the gravitational lensing of starlight by the sun's gravitational field. The position of the background stars, whose light grazed the surface of the eclipsed sun, was different in images taken during the eclipse and in images taken 6-months earlier, in the absence of the solar gravitational field in the line-of-sight. Gravitational lensing occurs when the gravitational fields of massive objects bend the path of passing light rays. More massive objects have stronger gravitational fields and therefore cause stronger gravitational lensing. We can measure the amount of lensing of galaxies behind clusters to map the mass within clusters.

Dark matter is found alongside baryonic matter and makes up the majority of mass in the universe. This is holds true in galaxy clusters. Therefore, dark matter within the clusters is primarily responsible for the shape distortion of background galaxy images. Light rays from separate ends of background galaxies passes through different parts of the cluster and are bent in slightly different ways by the different dark matter gravitational fields through which they pass. The majority of galaxies are lensed to an extent such that their shapes are only altered by roughly 1%. We refer to this small distortion effect as weak gravitational lensing (WL)**.** This level of distortion is only statistically detectable as an average shearing effect on a set background galaxies. Measurements of weak gravitational lensing rely on the valid assumption that galaxies along a line of sight are randomly oriented. WL shears the images of galaxies in a patch of the sky in the same direction. We therefore measure any cohesive alignment of background galaxy images as a WL signal.

The use of WL signals to map cluster dark matter is the preferred technique because it directly reflects the density distribution of matter and is model independent. In this research, we built two-dimensional dark matter maps of nearby galaxy clusters by measuring their WL signals. We compared the hot X-ray emitting gas and dark matter substructures within the clusters. Substructure comparisons can be used to learn about the formation history of clusters and the relative self-interactive qualities of dark matter and hot intracluster gas.

I am also contributing to an ongoing project to systematically map the surface mass density distribution of low-redshift clusters. This has only recently become possible with the creation of telescope cameras with large enough fields of view to capture the entire virial region of low-redshift galaxy clusters. All of our observations are from one such camera: the Dark Energy Camera (DECam) at the Cerro Tololo Inter-American Observatory's (CTIO) 4-meter telescope.[1] The camera spans 9.2 Mpc at redshift 0.06, roughly the average redshift of the clusters analyzed in this project. To process the images for each cluster, we are using software which is being developed for the upcoming LSST project at the Vera C. Rubin observatory. From the processed images, we measured the shapes of the galaxies behind our clusters and created dark matter surface density distribution maps for each of the clusters.

---

[1] We also retrieved X-ray images from the Chandra and XMM-Newton archives to map the distribution of hot X-ray emitting intracluster gas.

Background:

GR and Gravitational Lensing

General Relativity

Sir Isaac Newton formulated and published his universal law of gravity in the latter half of the 17th century. It successfully described gravitational interactions within the sphere of our everyday experience but didn't offer any explanation of the underlying mechanism of gravitational forces. It remained the primary description used for gravity until Albert Einstein proposed his theory of special relativity (SR) in 1905. The two theories were incompatible – Newtonian gravity states that changes in a system will instantaneously affect gravitational relations while SR requires that information not travel faster than the speed of light. Einstein set out to resolve this conflict in his theory of general relativity (GR).

In 1912, Einstein realized that an observer in a hermetically sealed box experiencing a downward force would have no way to determine whether the force was gravitational or due to an upward acceleration of the box. The fundamental connection creating this equivalence, Einstein determined, is curvature of space-time. Accelerated motion requires a curved spatial geometry as a consequence of the time dilation and Lorentz contractions described by SR. Since it is indistinguishable from accelerated motion, gravity must also be experienced in a curved spacetime. With this proposition, Einstein pried open the black box built of Newtonian gravity.

Einstein conjectured that massive bodies exert gravitational forces on other objects by warping the fabric of space-time in their vicinity. The analogy of a bowling ball on a rubber sheet is commonly used to aid visualization of this effect. A marble tossed onto the rubber sheet would have its linear trajectory bent by the warping around the bowling ball. In a similar fashion, massive objects in the universe curve the four-dimensional spacetime in their vicinity, creating a gravitational field. Nearby objects, including massless photons, feel the effect of the gravitational field as an added curvature in the local spacetime. Objects moving through spacetime travel along the shortest possible path, which in the case of a curved spacetime is curved. "According to this radical proposal, space is not merely a passive forum providing the arena for the events of the universe; rather, the shape responds to objects in the environment... As the eminent physicist

John Wheeler has often said in describing gravity, 'mass grips space by telling it how to curve, space grips mass by telling it how to move.'" (Greene, 2000)

The mathematical formalism of general relativity is largely contained in the Einstein Field Equations. These are a set of coupled, nonlinear, partial differential equations that relate the curvature of spacetime to the mass-energy content of the universe.

$$R_{\mu\nu} - \frac{1}{2}Rg_{\mu\nu} + \Lambda g_{\mu\nu} = \frac{8\pi G}{c^2}T_{\mu\nu}$$

where Λ is the cosmological constant, $R_{\mu\nu}$ is the Ricci curvature tensor, R is the Ricci curvature scalar, and $T_{\mu\nu}$ is the stress-energy tensor, which describes the mass and energy contents of spacetime. Of particular note, $g_{\mu\nu}$ is the metric tensor and describes how matter moves through space and time. We can define the Einstein tensor, $G_{\mu\nu}$, which describes the curvature at a specific point in spacetime as determined by the metric tensor:

$$G_{\mu\nu} \equiv R_{\mu\nu} - \frac{1}{2}Rg_{\mu\nu} + \Lambda g_{\mu\nu} = R_{\mu\nu} + (\Lambda - \frac{1}{2}R)g_{\mu\nu}$$

And in geometrized unit system, where $G = c = 1$, we can write a visually simplified version of the Einstein Field Equations:

$$G_{\mu\nu} = 8\pi T_{\mu\nu}$$

Though unnervingly short, this equation gets to the heart of the theory. The Einstein tensor, which describes curvature of spacetime as a function of the metric tensor, appears to be directly related to the stress-energy tensor, which describes the mass and energy contents of spacetime. In this way, the Einstein Field Equations show that gravity, via spacetime curvature, is created by the mass-energy contents of the universe and effects the spacetime trajectories of objects in the universe.

In order to test the theory of general relativity outside the realm of Newtonian mechanics, Sir Frank Watson Dyson conceived of an experiment to be carried out during the May 29, 1919 solar eclipse. During a solar eclipse, the light from the sun is blocked, but the solar mass still lenses passing photons. The degree of lensing is highest for stars whose light-rays graze the surface of

sun on their way to Earth. General relativity predicts that the deflection angle of an image passing a compact lensing source is:

$$\alpha = \frac{4GM}{c^2 b}$$

where M is the mass of the lensing source and b is impact parameter (the tangential distance between the original path of the light and the lensing object). GR predicts that images grazing the surface of the sun should be deflected by angle, α_{GR} :

$$\alpha_{GR} = \frac{4GM_\odot}{c^2 R_\odot} = 1.75"$$

Notably, Newtonian gravity predicts a lensing angle half as large, $\alpha_{Newton} \approx 0.875"$. During the 1919 eclipse, Sir Arthur Eddington carried out Dyson's experiment. He took photos of the apparent positions of stars whose light path grazed the surface of the eclipsed sun. He compared these images to pictures of the positions of the same stars from sixth months earlier, when their images weren't lensed by the sun's gravitational field. Eddington determined that the solar deflection angle was roughly 1.75 arcseconds, as predicted by GR. At the November 6, 1919 joint meeting of the Royal Society and the Royal Astronomical Society, it was announced that Eddington had observationally confirmed Einstein's 1915 angular deflection prediction based on his theory of general relativity.

In the century since it's proposal, no deviations from GR have been found. However, GR appears to be incompatible with the similarly well-tested theory of quantum mechanics. "The conflict alerts us to a fundamental deficiency in our conception of nature." (Greene, 2000)

Gravitational Lensing

According to Fermat's Principle, photons will travel along a path that minimizes their travel time. With the speed of light constant in the near vacuum of space, light simply travels the shortest path. However, as mentioned above, the shortest path in a curved space-time is not a straight line as it is in Euclidean space. The presence of mass-energy causes curvature in spacetime and, therefore, also bends the path of passing photons. In this way, massless photons are affected by gravity.

When light rays from a distant source passes by a massive object, referred to as a lens, the source's image is distorted. Lensing doesn't affect the surface brightness of a source because it involves no photon emission of absorption. However, because apparent size can change, a source's flux can be altered by lensing. There are, therefore, two observable disturbances to the source image. The change in apparent brightness, which is referred to as magnification, and the source's shape distortion, which is the lensing effect detected in this study.

Depending on the severity of the image distortion, we observe either a strong or weak gravitational lensing signal. Strong gravitational lensing can create multiple images of one source or dramatically bend its image into Einstein rings or arcs. Multiple images on one source are seen when more than one null geodesic[2] connects the world-line of the source to that of the observation. And specific geometrical alignments including incredibly massive lenses, allow us to observe the observe Einstein rings or arcs. In observations of lensing due to galaxy clusters, we only see Einstein arcs and rings created by the incredibly massive and dense centers of the clusters.

The majority of lensing occurs in the form of weak gravitational lensing (WL). Though the distortions in background images are too subtle to be directly seen, the weak lensing signal averaged over a set of source images is statistically detectable. To measure WL signals from galaxy clusters, we make the valid assumption that the orientation of the background galaxies is random and any that any coherent alignment is due to the gravitational field of the cluster. Generally, a weak lensing signal manifests as a shear of order 1% of the innate galaxy ellipticity.

We use measurements of the coherent alignment of the background galaxy images to reconstruct the gravitational field of the cluster and build a surface density map of the cluster's dark matter. Because the WL signals are so subtle, detecting them requires precise removal of instrumental and atmospheric signatures from the data. Most of time it took to build the lensing signal maps was spent removing the non-gravitational sources of image distortion. In later sections, I will describe the mathematical formalism of measuring the statistical shear from weak gravitational lensing and the process of removing other image distortion sources.

---

[2] The path of massless particles, like photons, is referred to as the null, or light-like, geodesic. It offers the shortest path within the geometry of the spacetime to a massless particle traveling at the speed of light.

Galaxy Clusters

Introduction to Galaxy Clusters

All of the research in this project is done on low-redshift galaxy clusters. In an astrophysics context, an object's redshift is a measure of its distance from us, both spatially and temporally, and these two measures are correlated because light travels at a finite speed.

Galaxy clusters are the largest gravitationally bound structures in our universe. They span distances of the order of a few Mpc and contain roughly 100-1000 luminous galaxies in addition to countless dwarf galaxies. Galaxy clusters are absolutely giant structures, with masses on the order of $10^{14} - 10^{15} \, M_\odot$. According to independent mass measurements of clusters using the velocity dispersion of their member galaxies and their X-ray emissions, only 10-15% of a cluster's mass can be accounted for by baryonic matter.[3] This requires that dark matter make up the remaining ~85% of cluster mass. Some estimates posit that ~20% of the mass is baryonic; roughly half in the form of hot intracluster gas and the other half contained in galaxies.

The core of many clusters is visually centered on a dominant central galaxy, or brightest cluster galaxy (BCG). BCGs are always giant ellipticals and are typically aligned with both the galaxy and the X-ray emitting gas distribution in the cluster. This property in the clusters involved in this work can be seen in Figure 16.

Why Conduct Galaxy Cluster Research?

Galaxy clusters are a key research tool for learning about phenomena on the scale of galactic evolution all the way up to the filaments that define mass structure on cosmic scales. Cluster research provides insight on galaxy formation, constraints on dark energy, and, most relevantly to this research, allows us to test cluster morphology predictions of our standard cosmological model.

The self-contained quality of clusters' deep gravitational potential wells allows us to study galaxy formation and how the process interacts with the intergalactic medium (IGM). We can

---

[3] Baryonic matter makes up the familiar and directly detectable cluster components: the stars, dust, and gas.

study the thermodynamics of the IGM and other intracluster gravitational and baryonic interactions.

On larger scales, the spatial distribution of clusters contains the enduring signature of the initial conditions and background cosmology of the universe. The evolutionary history of galaxy cluster number density and the properties of individual clusters (including their baryon content and degree of relaxation) are used set constraints on the initial density fluctuations of the early universe. Importantly, measurements of the number density of massive clusters as a function of redshift is also an important tool for setting constraints on the dark energy equation-of-state parameter.[4]

Most relevantly, the research done for this project is contributing to a body of information that can be used to test our current understanding of cluster formation, which is a prediction of our standard cosmological model. In the next section, I will discuss our standard cluster formation model and the roll of the research carried out in this project.

Galaxy Cluster Formation Models

Our standard cosmological model is the Lambda Cold Dark Matter model (CDM model). The CDM model predicts a hierarchical formation process that begins with the collapse of the initial overdensities in the early universe into small halos, which are large enough to overcome cosmological expansion. As with the rest of the universe, the mass of these halos is dominated by cold dark matter. These small halos then merge with one another, forming larger and larger structures. When the smaller collapsed objects accrete into more massive halos, they often survive the process as sub-halos within their new host for a long time. This formation model, therefore, predicts that dark matter halos, like galaxy clusters, should be rich in dark matter substructures.

Based on this formation model, we expect the fraction of cluster mass contained in substructures to increase with redshift. Clusters at higher redshifts should have larger portions of

---

[4] Dark energy is commonly described in terms of its equation-of-state parameter, w, which is determined by the dark energy density, ρ, and the dark energy pressure, p: $w = p/\rho$.

their mass contained in subhalos because the accretion rate of galaxies and galaxy group-sized halos is much higher in the earlier universe. Clusters at lower redshift will be smoother because they have had a longer time to reduce dark matter substructures through dynamical friction and to dynamically equilibrate. They also have a much lower number of actively infalling and merging subhalos. Observational research on cluster substructure as a function of redshift can inform our understanding of cluster formation and help test the CDM model on sub-megaparsec scales. My research is contributing to a growing catalog of maps of dark matter distribution in low-redshift ($0.04 < z < 0.1$) galaxy clusters. This growing body of information on low-redshift cluster morphology can serve as a baseline for comparison to higher-redshift cluster substructure studies.

The CDM hierarchical cluster formation model also predicts that clusters are built at the intersections of cosmic filaments and "sit at the largest nodes of the cosmic web." (Bartelmann & Schneider, 2001) West, Jones, and Forman confirmed this hypothesis in 1995. Models of large-scale structure confirm that matter doesn't flow evenly in all directions but, rather, moves "preferentially along filaments." (Squires et al., 1997) In fact, wide-field WL signal observations can expose the filaments along which mass accretes into clusters that are still undergoing formation processes. We observe the anisotropy of mass flows at large scales even in the centers of clusters. Here we observe the systematic alignment of brightest cluster galaxies (BCG) and the gravitational potential well of the clusters, which commonly correspond to the X-ray signal peak.

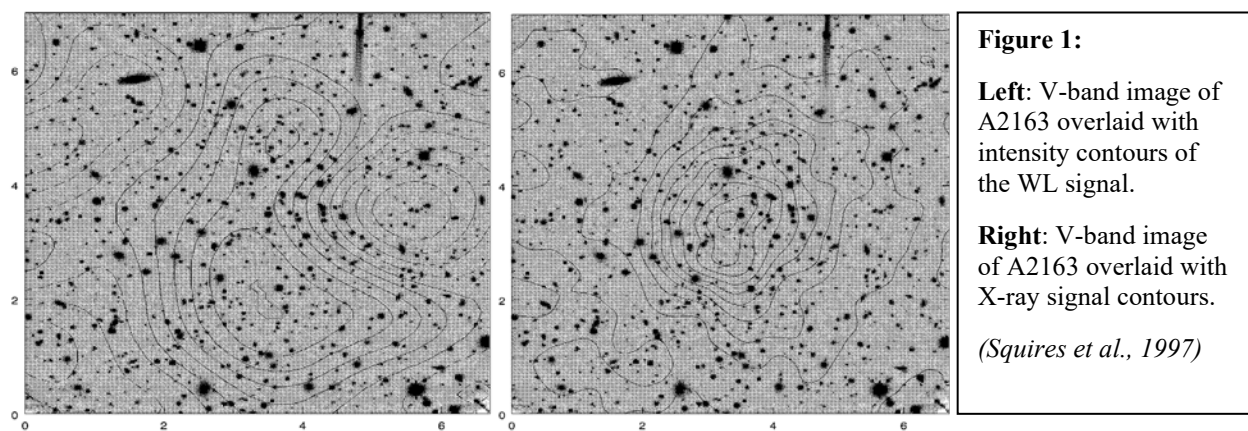## Cluster Morphologies and Implications on Dynamical State

Maps of a cluster's X-ray and weak gravitational lensing morphology can inform us about the cluster's recent mergers and its evolutionary formation history generally. It has been found that many clusters are still undergoing formation processes.

In a dynamically relaxed cluster, we expect the distribution of dark matter and hot X-ray gas to be determined by the cluster's gravitational potential well. Well-relaxed clusters are, therefore, observed to be regular, symmetrical and with a high degree of central concentration of both X-ray and WL signal intensity. Notably, local discrepancies between the depth of the potential well

and the intensity of the X-ray emissions can be created by shocks and waves which compress the intracluster gas, thereby increasing the local X-ray emissions.

Galaxies still undergoing formation processes exhibit irregular morphologies, most commonly detected as significant substructure in WL and X-ray observations. In these cases, subhalos within the cluster are still intact and possibly interacting. In particular, an offset between X-ray and WL detected substructures is a tell-tale sign of ongoing cluster formation. Discrepancies in the location of the peak X-ray and WL signals can occur because dark matter halos are able to pass through each other while gas clouds are collisional and get left behind.[5]

One example of a cluster with significant offset in the position of the WL and X-ray signal peaks is A2163 ($z = 0.201$). In 1997, Squires observed that both the shear-selected substructure and the visible galactic luminosity of A2163 shared two peaks in the cluster core. Interestingly, Squires also found that the X-ray signal had a relatively regular appearance and one centrally located peak. This discrepancy between the WL and X-ray morphologies, alongside the lack of any optical peak at the X-ray centroid, strongly indicate that A2163 is still reeling from a recent merger. This offset can be physically explained by two colliding sub-halos that fell into the cluster center, passed through each other, and are now moving toward each other once again. The two WL signal peaks might then be the "relics of the central regions of the two former subclusters." (Squires et al., 1997) The self-interacting X-ray gas from the subhalos would have collided on their first pass through one another and gotten stuck in the central location. This interpretation is corroborated by numerical cluster formation simulations. The hydrodynamical N-body simulations conducted by Schindler & Mueller (1993) predict that we would have

Figure 1:

Left: V-band image of A2163 overlaid with intensity contours of the WL signal.

Right: V-band image of A2163 overlaid with X-ray signal contours.

(Squires et al., 1997)

---

[5] The classic example of this is phenomena is the bullet cluster. There are many other clusters that show this offset, including A2163.

observed the centers of the interacting subclusters and the local X-ray gas distribution as overlapping for the bulk of infall process. Once the subclusters had passed through one another, however, they predict we would detect the former subhalo centers as distinct mass density peaks and measure a smooth X-ray signal with one central peak. The simulation's cluster description at this stage bears an uncanny resemblance to Squires' observations of A2163.[6]

Galaxy Clusters as X-ray Sources

After all this discussion of X-ray substructure, it is worth briefly examining X-ray emissions from clusters. Galaxy clusters are the most luminous X-ray sources in the sky, with X-ray luminosities on the order of $10^{43} - 10^{45} ergs^{-1}$. A cluster's total X-ray luminosity is related to its mass. The primary source of the X-ray emissions is Bremsstrahlung radiation (from free-free interactions) within the hot intracluster medium (ICM). The ICM is a plasma with $10^7 K \leq T_{ICM} \leq 10^8 \ K$ and a density on the order of $\sim 10^{-3}$ particles/cm³. The source of the X-ray emitting intracluster gas is mixed. The metallicity of the gas is roughly a third of the solar metallicity, indicating that at least some of it was born from stars and galaxies within the cluster. However, some of the gas has also likely been around since the early days of the cluster's formation and was heated through time by shock waves from mergers and gas falling into the cluster potential. Line emissions from heavily ionized iron and other heavy elements contributes a small amount to the clusters' X-ray luminosity.

The intensity of X-ray luminosity from bremsstrahlung radiation scales quadratically with the density of the ICM, meaning that local ICM overdensities correspond to increased X-ray emissions.[7] This relation also dictates that these density fluctuations, which we are trying to map,

---

[6] As of 1997, A2163 had the most luminous and extended radio halo ever detected. Notably, Burns et al. (1994) found the same substructure pattern as A2163 and a substantial radio halo in another cluster: A2255. Squires et. al (1997) remarked how the few clusters which had been found with appreciable radio halos all showed evidence of recently experiencing a merger. (These include A2163, A2256, A2255, and the Coma cluster. (Squires et al., 1997)) More recently, Cassana et al. (2010), Cuiciti et al. (2015), and Donahue et al. (2016) described how giant radio halos are another signature of ongoing cluster mergers and formation. One of the other clusters with both irregular morphology and a large radio halo is the Coma Cluster ($z = 0.0236$). See Appendix A for more information on the Coma Cluster substructure.

[7] Because of this strong dependence on the density, X-ray measurements aren't as susceptible to line-of-sight projection effects as other cluster observation methods.

are easiest to detect in the densest region of the cluster: the core. Local overdensities are caused by areas of increased gravitational potential, which surround galaxies and subhalos, as well as by the pressure and shock waves created by infalling subhalos. We use images of the X-ray emissions of our galaxy clusters taken by the Chandra and XMM-Newton cameras. The images show the X-ray luminosity distribution and, therefore, ICM surface density distribution across the central region of the clusters.

Galaxy Clusters Mass Measurement Methods

Like substructure analysis, measurements of galaxy cluster mass offer cosmological insights. Accurate cluster mass measurements are an important source of constraints on the current mean mass density of the universe. They also provide information on the spatial distribution of mass on cosmic scales and the growth of structure on cosmological timescales.

We have three main methods for determining galaxy clusters' masses. The first method, chronologically, employs the virial theorem to relate the observed velocity dispersion of the cluster galaxies to the depth of the cluster's gravitational potential well. This mass measurement technique is aptly called the *virial mass*, M_v .[8] Once adequate X-ray telescopes were available, physicists began using the X-ray emission intensity of clusters as a proxy for their mass. Measurements of the *X-ray cluster mass*, M_x, rely on the assumption that clusters are spherically symmetric and that the ICM is in hydrostatic equilibrium with the clusters' gravitational potential wells. The degree of substructure in a cluster therefore has implications for the accuracy of the mass measurements based on its X-ray luminosity. Earlier, I discussed how observations of cluster morphologies have shown that many clusters are far from relaxed and, therefore, don't match the assumptions required for X-ray cluster mass measurements. In his 1997 paper, Squires elaborated on this: "since the dynamical timescale for the formation of clusters is comparable to the Hubble time, and as many clusters are found to have substructure

---

[8] By measuring the velocity dispersion of galaxies moving within the cluster's potential well, one can determine the average kinetic energy of each galaxy, treated as a particle. The galaxies' kinetic energy can then be related to their gravitational potential energy (due to the mass of the cluster), using the virial theorem: $E_k = \frac{-E_p}{2}$. Comparisons of the virial mass estimates for clusters to the known mass/light ratio of its baryonic constituents indicate that there must be enormous amounts of dark matter in clusters.

implying that they are dynamically young and unrelaxed, the X-ray mass derivations are not without uncertainties."

More recently, high resolution telescope cameras have made possible a third independent method of measuring cluster mass. The method, which was used in this research, relies on the WL signal from clusters to determine their *lensing cluster mass*, M_{lens}. WL detections have rapidly become the standard tool for measuring cluster mass because there are no assumptions about the dynamical state of the cluster or its components involved in the calculations. The largest downside to this method is the observational difficulty of measuring the WL signals from clusters. Jacqueline McCleary, a former PhD student in Professor Dell'Antonio's lab, described: "The distortion of background galaxies induced by the intervening cluster is much smaller than the intrinsic uncertainty of galaxy shape measurement." (McCleary et al., 2015) We can overcome this challenge by, first, diligently removing sources of non-lensing shape distortions from our images. Second, we further minimize the shape uncertainty by measuring the statistical gravitational shearing across a large numbers of background galaxies.

Theoretically, we expect to calculate the same mass for a dynamically relaxed cluster using all three of the measurement methods. Of course, this frequently doesn't happen, so the size of their discrepancies is used to learn more about the internal structure of the cluster. Comparisons of M_v and M_{lens} show that they are frequently in relatively close agreement, which indicates that the intracluster DM particles and cluster galaxies have roughly the same velocity dispersion. It also reveals that the distribution of optical galaxies traces the potential well, which is largely defined by the dark matter distribution. Generally, some disagreement is found between M_{lens} and M_x, with M_x being systemically lower than M_{lens}. While M_{lens} offers a measurement of the cluster mass without relying on any assumptions about the dynamical or compositional state of the cluster, M_x assumes that the ICM is in hydrostatic equilibrium with the gravitational potential well. M_x can be influenced by local temperature and density variations in the ICM, which are created by variable mass densities as well as turbulence, shock waves, and magnetic fields. The fact that these mass measurements often disagree can be taken as further evidence that many clusters are not yet virialized. And, despite their consistent differences, it has been found that these three estimates are generally consistent to within roughly a factor or two. (Bartelmann & Schneider, 2001) Ultimately, even if a cluster's X-ray luminosity isn't an ideal

tool for precise mass measurements, it is still a strong predictor of the cluster mass. In Appendix B, I elaborate on the specific comparative mass findings of a series of research projects. Combining the general thread of these findings with the hierarchical formation model, we can expect greater discrepancies between M_{lens} and M_x at higher redshifts, where cluster evolution is further behind.

Dark Matter: Repeated Discoveries

Though these three methods for measuring cluster mass don't always agree, they all show that the baryonic components of the cluster can't possibly account for its whole mass. The existence of large quantities of dark matter is generally thought to make up the difference. Ultimately, ~85% of the cluster mass we are mapping and measuring using weak gravitational lensing signals is dark matter. It is, therefore, worth diving into a brief introduction to dark matter.

While creating the first systematic catalogs of nebula, Charles Messier and William Herschel observed their propensity to cluster. Throughout the nineteenth and early twentieth century, larger numbers of nebula continued to be recorded and the grouping pattern became even clearer. Then, in the 1920s, Edwin Hubble proved that spiral and elliptical nebula are full-fledged galaxies, like the Milky Way. This discovery implied that the clusters of nebulae were in fact unimaginably massive structures: clusters of galaxies. In 1931, Hubble and Humason measured the velocities of galaxies within the Coma Cluster and found that their velocity dispersion was huge; on the order of ~1,000 km/s. The mass contributed to the cluster by the galactic stars and gas was clearly insufficient to prevent the galaxies, with such a high velocity dispersion, from rapidly escaping the cluster. Operating under the assumption that the cluster was in virial equilibrium, they calculated the minimum mass of the cluster required for it to remain a gravitationally bound system. They found that the mass needed to be $\sim 200 - 400$ times larger than the cumulative mass of the cluster's stars. Zwicky also found that the gravitational potential experienced by the galaxies in rich clusters was on the order of 10 to 100 times larger than could

be accounted for by the luminous galaxies themselves.[9] This led Zwicky to propose that the remaining mass was provided by large quantities of some form of *dark matter*, inventing the popular name in the process. "This was the earliest indication that there is invisible mass, or dark matter, in at least some objects in the Universe." (Bartelmann & Schneider, 2001)

Dark matter is also required to explain the orbital speeds of stars in spiral galaxies. If all, or most, of the mass within a galaxy was contributed by the stars, the orbital velocity should fall off as $\sim \frac{1}{\sqrt{R}}$ at large radii. In 1971, Vera Rubin and Kent Ford measured the doppler-shift of the 21-cm line emission from M31 (Andromeda). They determined that the disk had a nearly constant orbital speed of $\sim 230 \ km/s$ out to a radius of $35 \ kpc$, which is nearly six times the scale radius of the galaxy. This observation implied the existence of some galactic mass source beyond the stars and gas. Rubin and Ford proposed that the stellar disk sits within a dark matter halo. Further research determined that nearly all spiral galaxies have a fairly constant orbital speed, which implies the existence of dark halos much larger than the visible disks in all spiral galaxies, not just in M31.

The natural next question is: What is dark matter? Since WL measurements aren't influenced by the composition of the dark matter (or of the cluster mass at large), I will only briefly elaborate on this. It was originally posited that the dark matter in galactic halos might be comprised of Massive Compact Halo Objects (MACHOs), including cold white dwarfs, black holes, brown dwarfs, and other dim compact objects. Measurements of the gravitational lensing signal from dark matter in the Milky Way determined that no more than 8% of the Milky Way's dark matter could be contributed by MACHOs. We now believe that the galactic dark matter is a smooth distribution of nonbaryonic material and not dominated by a scattering of MACHOs.

The list of remaining dark matter candidates includes the following:

1) Very low mass elementary particles called Axions. (50 billion axions have the mass of single electron)
2) Primordial blackholes, with masses up to $10^5 \ M_\odot$, have also been suggested.[10]

---

[9] Large amounts of dark matter are also integral to understanding how the X-ray emitting intracluster medium remains bound to the cluster. If clusters only contained the mass of their luminous galaxies and the ICM itself, the gas would have dissipated into the intercluster regions a long time ago.

[10] "It is a sign of the vast ignorance concerning nonbaryonic dark matter that two candidates for the role of dark matter differ in mass by 76 orders of magnitude." (Bartelmann & Schneider, 2001)

3) Neutrinos, which we are nonbaryonic, have a non-zero mass, and have been detected on Earth, are a dark matter candidate. However, if neutrinos were responsible for all of the nonbaryonic mass in the universe, each would need a mass (~3.8 eV) much larger than the upper constraint ($0.019 \ eV < m_v c^2 < 0.1 \ eV$) that has been experimentally determined. Because of these mass constraints, we know that neutrinos could make up at most 3% of the DM mass.

4) Weakly Interacting Massive Particles (WIMPS) are also being considered. They belong to a supersymmetric model (extension of the standard model) and are essentially any particle that interacts using the weak nuclear force and is more massive than the upper bound on the neutrino mass. Like neutrinos, WIMPS would be incredibly difficult to detect because they only interact through the weak nuclear force and gravity. However, WIMP detectors have been built because WIMPs should sometimes interact with atomic nuclei. At this point, no WIMPs have been detected.

Though my work doesn't shed insight onto what the constituents of dark matter are, I am still able to map its presence in galaxy clusters because of its gravitational effects on passing photons.

Mathematical Descriptions of Weak Gravitational Lensing

Weak Lensing Equation

In the curved spacetime of general relativity, we have multiple definitions of distance. We use the Angular-Diameter distance in Weak Lensing equations. It relates an object's physical size (cross section dA) and its angular size (solid angle in sky) to the object's distance (or redshift) from an observer. The intensity of a weak lensing signal depends on the surface mass density distribution of the lens, the angular diameter distance to the lens, D_d, the angular diameter distance to the background source, D_s, and the angular diameter distance between the two, D_{ds}.

Calculations of the deflection angle of a galaxy image due to the mass distribution of a cluster relies on a few assumptions. First, we assume that there aren't other lenses along the line-of-sight to the background galaxy. If we determine that there are, we must measure and remove their signal during data processing. Second, we approximate that a galaxy cluster is a *geometrically thin lens,* with all of its lensing components at the same D_d. We also assume that the extent of the cluster is significantly smaller than D_d and D_s. This is a reasonable assumption, because a standard galaxy cluster is a few Mpc across and the average redshift of the clusters analyzed in this project is 0.068, corresponding to $< D_d > \cong 270 \ Mpc \ (< z > = 0.068)$. This

series of assumptions allow us to approximate the lens and source as coplanar and to describe the source light rays, which are smoothly bent in the region surrounding the cluster, as two straight rays with a sharp bend near the cluster. We call the angle at the bend the *deflection angle, $\hat{\alpha}$*.

We consider the lensing configuration shown in Figure 2:

- η is the physical position of the background galaxy (the source) in the plane at D_s (called the *source plane*).
- β is the physical angular position of the source. This is the source angular position we would measure in the absence of a foreground lensing cluster.

Using the small angle approximation, we can build the following geometric relation:

$$\beta = \eta/D_s$$

- ξ is the impact parameter. It gives the shortest distance between the source's light ray and the lens. The lensing parameter also describes the position of the source's image in the lens plane. Much like the source plane, the lens plane is the 2-dimensional region surrounding the lens at D_d.
- θ is the observed angular position of the source.

Once again, the small angle approximation allows us to relate physical quantities:
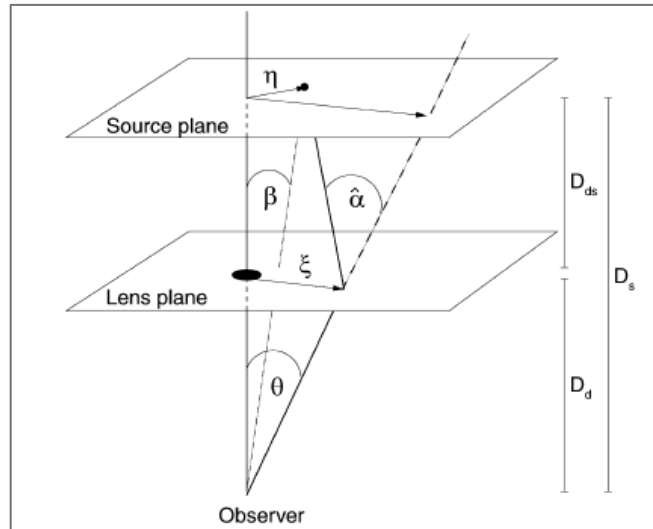
$$\theta = \xi/D_d$$

We can build the following geometric relation from the similar triangles in Figure 2:

$$\frac{D_s}{D_d} = \frac{\eta + D_{ds}\hat{\alpha}(\xi)}{\xi}$$

Figure 2: This figure shows the weak lensing set-up we are referencing while deriving the weak lensing equation. *(Bartelmann & Schneider, 2001)*

By mixing these three equations, we transform the equality above into an equation relating the true angular position, β, of a source to its apparent angular position, θ. This yields *the lens equation:*

$$\beta = \theta - \frac{D_{ds}}{D_d}\hat{\alpha}(\xi)$$

In the section on general relativity (see page 9), I gave the equation for a deflection angle due to a point source lens. Einstein used the equation to find the general relativity predicted deflection angle of a background star during the 1919 solar eclipse. The point lens deflection angle, also called the Einstein angle, is given by:

$$\alpha = \frac{4GM}{c^2 \xi}$$

In the weak lensing regime, we can linearize the deflection angle. The total deflection angle due to a discontinuous extended lensing source is the linear superposition of the lensing angles from each piece of the lens, i:

$$\hat{\alpha}(\xi) = \sum_i \hat{\alpha}_i(\xi) = \sum_i \frac{4GM}{c^2} * \frac{\xi - \xi_i}{|\xi - \xi_i|^2}$$

where ξ_i is the impact parameter between the mass element m_i and the source's light ray. (It is also the position of the mass element m_i on the lens plane.)

Since the surface mass density of galaxy cluster is continuous, we integrate over the mass element, $dm = \Sigma(\xi)d^2\xi$, where $\Sigma(\xi)$ is the spatially variant surface mass density of the lens. The deflection angle for a cluster, or any source with a continuous mass distribution, is:

$$\hat{\alpha}(\xi) = \frac{1}{\pi} \int \Sigma(\xi') \frac{\xi - \xi'}{|\xi - \xi'|^2} d^2\xi'$$

Together, the lensing equation and this deflection angle, relate the true and apparent angular positions of a background galaxy lensed by a continuous cluster. By defining the scaled deflection angle, $\alpha(\theta)$, we are able to further simplify the lens equation:

$$\alpha(\theta) \equiv \frac{D_{ds}}{D_d} \hat{\alpha}(\xi) = \frac{D_{ds}}{D_d} \hat{\alpha}(D_d\theta)$$

For a continuous lens:

$$\alpha(\theta) = \frac{1}{\pi} \int \kappa(\theta') \frac{\theta - \theta'}{|\theta - \theta'|^2} d^2\theta'$$

where $\kappa(\theta')$ is the dimensionless surface mass density, or convergence, defined by:

$$\kappa(\theta') = \frac{\Sigma(\xi')}{\Sigma_{crit}}$$

Σ_{crit} is the critical surface mass density, which is dependent only on the angular diameter distances between the observer, the lens, and the source:

$$\Sigma_{crit} = \frac{c^2}{4\pi G} * \frac{D_s}{D_d D_{ds}}$$

Finally, we rewrite the lensing equation:

$$\beta = \theta - \alpha(\theta)$$

By using equations above, we can relate the physical angular position of a background galaxy with its observed angular position, the surface mass distribution of the cluster, and the ratio of the angular diameter distances to the source, the lens, and in between the two.

In our research, we are trying to determine the relative surface mass density across the virial region of a cluster and, therefore, observe the cluster's dark matter substructure. This equates to finding $\kappa(\theta)$, which is the dimensionless surface mass density, commonly referred to as the convergence.

Observing Weak Lensing Signals

In general, we describe the mass distribution of a lensing source in terms of its surface mass density, Σ, or its dimensionless convergence, κ. Cases of strong gravitational lensing are characterized by $\kappa \geq 1$ and are generally only observed near the dense cores of clusters. Weak gravitational lensing, on the other hand, creates distortions in the background galaxy images that are significantly smaller than the images themselves. Because the entire virial region of galaxy clusters produces WL signals, this project and most lensing research of galaxy clusters are carried out in the WL regime, which is characterized by $\kappa < 1$.

Weak gravitational lensing alters both the shape and size of background galaxy images. We would ideally directly measure the lensing convergence, κ, but convergence alone creates an

isotropic magnification of the background galaxy image. Since we don't know the apparent size of the galaxies in the absence of a lensing cluster, we can't explicitly measure their magnification. The tidal forces from the cluster's gravitational field also cause a shear, γ, which is observed as a distortion of the image shape. Importantly, we know the that in the absence of a lens we would measure no coherent shear pattern across a set of galaxies. Background galaxies are randomly oriented, meaning that any measurements of coherent alignment are detections of a lensing effect. The gravitational potential creates a curl-free shear, stretching the galaxy images tangentially from the lens. This allows us to determine the intensity of the shear by measuring the tangential ellipticity of the galaxies:

$$e_{tan} \cong 2\gamma$$

By defining the angle by which background galaxies are tilted to the image axis as θ, we can decompose the galaxy shape into its elliptical moments:

$$e_1 = e * \cos(2\theta) \, ; \; e_2 = e * \sin(2\theta)$$

where e_1 is the projection of the ellipse onto the x- and y-axes and e_2 is its projection onto the lines $x = y$ and $x = -y$. We define the tangential ellipticity in terms of these elliptical moments:

$$e_{tan} = -(e_1 \cos(2\phi) + e_2 \sin(2\phi)) \cong 2\gamma$$

where ϕ is the azimuthal angle (measured clockwise from north) from the determined lens center to the source galaxy.

Because both the convergence and the shear are derivatives of the deflection angle (and second derivatives of the gravitational potential), there's an integral relation that maps one into the other. Their relationship through deflection angle, α, is seen in the Jacobian matrix, A, which contains the first order partial differentials of the lensing equation:

$$A(\theta) = \frac{\partial \beta}{\partial \theta} = \begin{pmatrix} 1 - \kappa - \gamma_1 & -\gamma_2 \\ -\gamma_2 & 1 - \kappa + \gamma_1 \end{pmatrix}$$

An integral of the measured shear yields the sum of the convergence and a constant of integration. We map this result as a function of position on the projected map of the cluster. This map shows the relative surface mass density across the galaxy cluster because the constant of

integration only effects the baseline. We use a program called Fiatmap which uses this relationship to turn shape measurements of the background galaxies into relative surface mass density maps of the clusters.

Fiatmap produces both an E-mode and B-mode map. As in electromagnetism, we can decompose the shear tensor field into a curl-free component and a curl-like component. The curl-free component, analogous to the electric field and thus called the E-mode signal, measures the degree to which galaxies have been stretched radially from each point. Because the gravitational potential creates a central force, the weak lensing signal manifests entirely as an E-mode signal. The E-mode map is, therefore, the two-dimensional mass density map of our cluster. The corresponding curl-like component of the shear, comparable to the magnetic field and thus called the B-mode, should have no systematic signal. The B-mode map shows the curl-like ellipticity (which is e_{tan}, rotated by $\pi/4$ radians): $e_c = e_2 \cos(2\phi) - e_1 \sin(2\phi)$

We do generally see a signal in the B-mode map, even though the WL creates no curl-like shear. The signal isn't from the gravitational potential well structure of the cluster but is the signature of some systematic error or noise. We create B-mode maps to measure the biases in our measurements that appear in both the E- and B-modes, so that we can remove them from our E-mode findings.
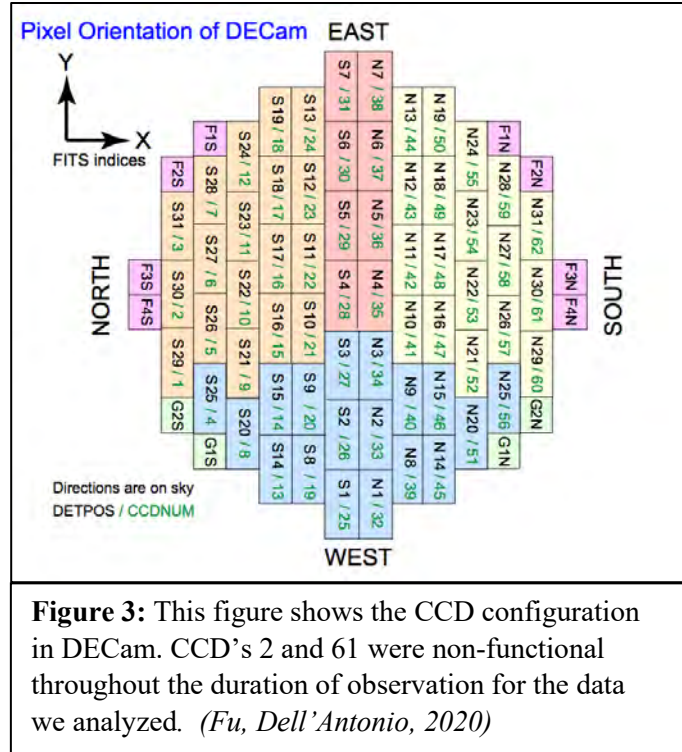
$\bullet\bullet\bullet$

The ongoing project, to which I am contributing, is systematically creating mass maps for low-redshift galaxy clusters. This has only recently become possible with the creation of telescope cameras with large enough fields of view to capture the expansive virial region of low redshift galaxy clusters. In the past two decades, there has been an emergence of large-scale surveys with wide fields of view and increased detection of faint objects. The Sloan Digital Survey and the Gaia Survey, both of which we use as reference catalogs in our data processing, are examples of these surveys. All of the observations we use are from one wide-field and deep seeing camera: the Dark Energy Camera (DECam) at the Cerro Tololo Inter-American Observatory 4-meter telescope. We used the data processing pipeline that is being developed for use by the Legacy Survey of Space and Time (LSST) that will produce images with unprecedented depth and field-of-view.

NOAO and DECam:

The data we used for our research was retrieved from the National Optical Astronomy Observatory's (NOAO) Science Archive. We collected raw images and master calibration files taken by the wide-field Dark Energy Camera (DECam) on the 4-meter telescope at the Cerro Tololo Inter-American Observatory [a division of NOAO]. The DECam imager was designed and built between 2004 and 2010. As of 2012, it was the world's most powerful digital camera. And in the phenomenal atmospheric conditions of the Chilean Andes, DECam took the deepest wide-field astronomical images to date. (Kim, 2012) DECam was built primarily to conduct the Dark Energy Survey (DES), which was an international effort carried out by more than 130 scientists from 27 separate institutions. The DES and ongoing projects have used DECam to observe hundreds of millions of galaxies.

In order to accomplish its science goals, DECam requires a large field of view and high sensitivity to redshifted light from distant galaxies. It is comprised of 62 CCD's, 60 of which were functional throughout the period of observations used in this research. When an image is taken simultaneously in each of the CCD's, the output is referred to as a "visit." In all the visits we analyzed, CCD's 2 and 61 were non-functional. As can be seen in Figure 3, these non-

functional CCD's image the far northern and southern parts of the sky, respectively. Each CCD is 2048x4096 pixels and the camera contains 520 megapixels total. Each pixel images 0.265" and the complete camera has an expansive 2.2-degree field of view. [11] This small pixel-scale and wide-field of view made DECam the obvious choice to use in our project of mapping weak gravitational lensing signals from low-redshift galaxy clusters. At a redshift of 0.06, the camera can image across 9.2Mpc of sky.

Figure 3: This figure shows the CCD configuration in DECam. CCD's 2 and 61 were non-functional throughout the duration of observation for the data we analyzed. *(Fu, Dell'Antonio, 2020)*
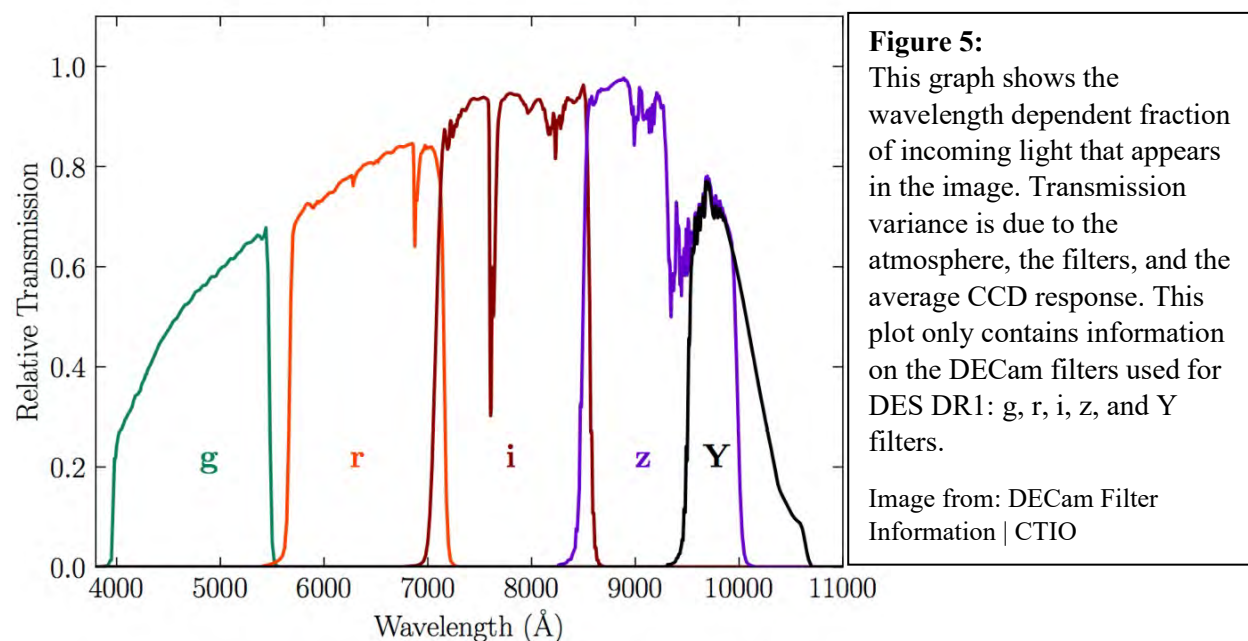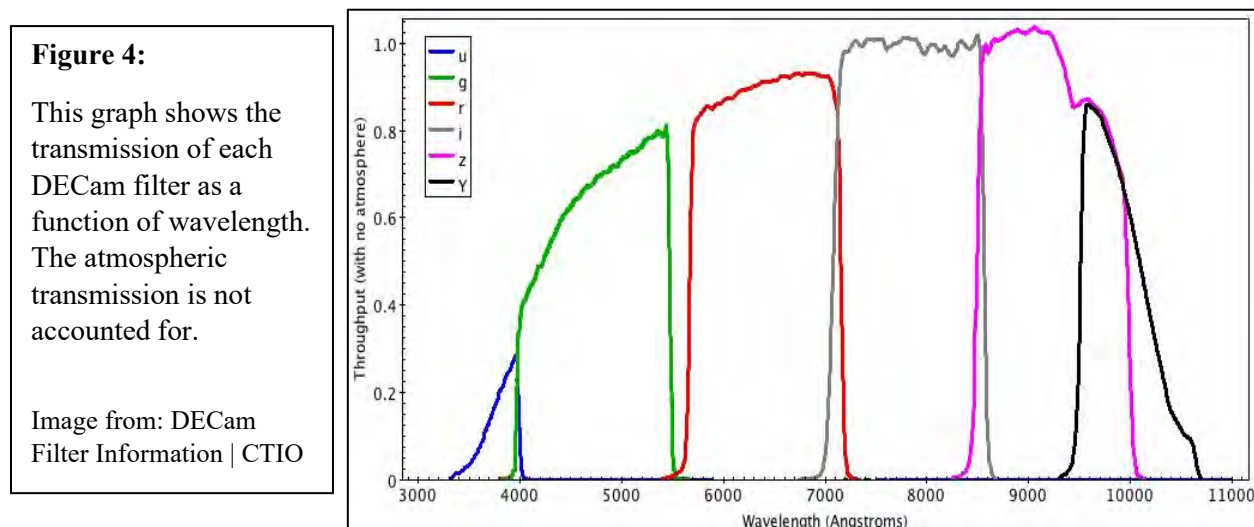
DECam images are taken through a series of six filters: u, g, r, i, z, Y. We analyzed each cluster in the u, g, r, i, and z filters and used Y-band images when they were available. The wavelength range of each filter is as follow (in Angstroms):

- u: $3340 - \sim4060$
- g: $3800 - 5650$
- r: $5400 - 7350$
- i: $6750 - 8700$
- z: $8250 - 10150$
- Y: $9300 - 10700$

Figures 4 and 5 show the transmission through each DECam filter as a function of wavelength. The instrument is most sensitive in the r-band, followed by the i-band. The r-band "also optimizes the balance between high background galaxy luminosity and reasonably low sky noise (both of which increase in increasing wavelength)." (McCleary et al., 2015) Dependent on which band's images have the most cumulative exposure time and the cleanest seeing, either r-band or i-band images are used to measure the weak gravitational lensing signal.

---

[11] More precisely, central pixels each image 0.2637" and pixels near the edge image 0.2626".

The galaxy cluster sample in this project includes 7 low-redshift clusters, $< z > = 0.068$, with varying masses and X-ray luminosities. Their individual properties are laid out in Appendix C and information about the data we used for each is shown in Table 1. Many of the images we used were collected as part of the umbrella project by Professor Ian Dell'Antonio, Jacqueline McCleary, and Shenming Fu. The data analysis on the clusters has been conducted in collaboration with Shenming Fu, Ian Dell'Antonio, Andrea Minot, and Nick Conroy.

Figure 4:

This graph shows the transmission of each DECam filter as a function of wavelength. The atmospheric transmission is not accounted for.

Image from: DECam Filter Information | CTIO

Figure 5:
This graph shows the wavelength dependent fraction of incoming light that appears in the image. Transmission variance is due to the atmosphere, the filters, and the average CCD response. This plot only contains information on the DECam filters used for DES DR1: g, r, i, z, and Y filters.

Image from: DECam Filter Information | CTIO

Average Exposure Time (s); Total Exposure Time (s)	u	g	r	i	z	Y
A3376	450; 2700	400; 3200	400; 6000	500; 3600	450; 2500	*No data*
A3827	236; 4720	178; 3383	225; 8335	190; 5140	127; 5330	133;2530
A3667	223; 8460	136; 4070	151; 4530	189; 2840	204; 1840	51; 305
A2457	500; 7500	294; 4410	300; 6900	300; 3000	275; 6060	*No data*
A3822	407; 4878	175; 2625	215; 3230	137; 5360	146; 2620	132; 2895
A3695	187; 2620	146; 730	191; 1530	201; 1405	144; 3310	151; 3920
A85	441;7060	360; 1800	270; 4860	247; 3760	*No data*	*No data*

Table 1: This table contains information on data obtained for each cluster in my sample. Longer total exposures times create are deeper coadded images. However, when single exposures are too long, the risk of bright star saturation high. Saturated stars make calibrating the exposure more difficult. Generally, the r- or i-band has a particularly long total exposure time, because it is the band meant to be used for the shear shape measurement.

LSST:

Before June of 2019, the DECam Community Pipeline was the best method for processing the raw images taken by DECam. However, the creation of the LSST Science Pipelines, particularly the obs_decam pipeline, has changed this. The LSST Science Pipelines are being developed for use on data from the NSF Vera C. Rubin Observatory[12] (previously known as the Large Synoptic Survey Telescope, LSST). Obs_decam is a package within the pipeline specifically designed to handle data from DECam and is a state-of-the-art tool for processing the optical and near-infrared images. The same general image procedure is applied in all of the LSST Pipeline packages, so the processing steps we used will also be used on images from the Rubin Observatory.

The main task of the Vera C. Rubin Observatory will be to carry out the Legacy Survey of Space and Time (LSST). The project aims to provide datasets for 4 main lines of research: "understanding the mysterious dark matter and dark energy, hazardous asteroids and the remote solar system, the transient optical sky, [and] the formation and structure of the Milky Way." The survey will be incredibly important to research on the dark matter structure of nearby galaxy clusters because it will produce the necessary deep wide-field multicolor images with high image quality and deep seeing for shear measurements and accurate photometry in at least 5 bands to measure photometric redshifts. (About LSST | Legacy Survey of Space and Time) In order to address all its complex research goals, the LSST will survey the entire sky every few nights for ten years with unprecedented depth and field of view. It is expected to come online in late 2022.

From its location in north-central Chile, the Vera Rubin Observatory will capture exposures used to create what will be the deepest and widest image of the night sky. The 8.4-meter Simonyi Survey Telescope will have the effective light-gathering ability of a 6.7 m diameter primary mirror and in each 30 sec exposure will be able to capture objects that are 10 million times too faint to be seen with the naked eye. The 3200-megapixel camera (recall, DECam is a 520-megapixel camera and is the current state-of-the-art) will take images that each span 96 square

---

[12] It was announced on January 6, 2020 that the Large Synoptic Survey Telescope would be renamed the NSF Vera C. Rubin Observatory, after the woman credited with observationally discovering the need for dark matter in spiral galaxies. Notably, the NSF Vera C. Rubin Observatory is the first national U.S. observatory to be named after a woman.

degrees. This is an area the size of 40 full moons. For comparison, each DECam image contains 3 square degrees of the night sky. Each night the telescope will take 1000 pairs of exposures of the sky, accumulating observations of 37 billion stars and galaxies in its 10 years of operation. Each week, the whole sky will be imaged twice and over the course of ten years, each region of sky will have been imaged 1000 times.

> "The LSST will be unique: no existing telescope or proposed camera could be retrofitted or re-designed to cover ten square degrees of sky with a collecting area of forty square meters. [LSST was] named the highest priority for ground-based astronomy in the 2010 Decadal Survey…" (The Large Synoptic Survey Telescope | Rubin Observatory)

Beyond the hardware, the final necessary component of the project includes a data management system, the preliminary version of which we are using. The development of a strong data analysis pipeline for the upcoming LSST is very important, because the telescope will be collecting enormous amounts of data. Due to the depth of the images and the speed with which they will be collected, roughly 20 terabytes of raw data will need to be processed and stored on a nightly basis. In the ten years that the Vera Rubin Observatory is planning to operate the Legacy Survey, scientists anticipate that approximately 60 petabytes of data will be collected and consequently need to be addressed. After raw data processing, the project is expected to produce roughly 500 petabytes of information. (About LSST | Legacy Survey of Space and Time) In the next section, I will discuss how we are using the data processing software, being designed to take on this challenge, to work through images collected by DECam.

Methods

Shenming Fu wrote an incredibly detailed and helpful manual for using the LSST Science Pipelines obs_decam program to process DECam data collected from the NOAO Science Archive. His manual and willingness to answer my questions were key to my understanding this processing procedure. The steps I will describe below are instructionally outlined in the document written by Fu and in the LSST Science Pipeline's "Getting Started Tutorials." (Shenming Fu, Ian Dell'Antonio, 2020; Getting Started with the LSST Science Pipelines — LSST Science Pipelines.)

The LSST pipeline is most easily broken down into the three steps shown in the flowchart:

1) Processing and calibrating individual exposures
2) Coadding the processed exposures of each band
3) Building a cohesive multiband catalog of all the light sources in the images

In order to run the LSST Science Pipeline, it must be downloaded and called upon in the working directory. We ingest (or link) a file called "_mapper" into our data repository which tells the LSST pipeline that we will be using the obs_decam package. We also download raw images and master calibration files from the NOAO science archive, as well as a set of reference catalogs, and ingest these all into the working directory.
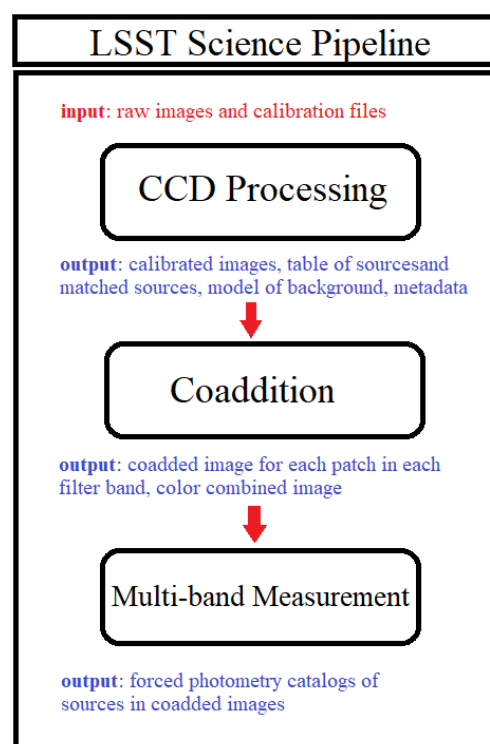
1) Processing/Calibrating individual exposures

The first phase of the image processing is dominated by a python script in the LSST Science Pipeline called processCcd.py. This python script performs three main image processing phases: instrumental signature removal (ISR), characterization of the image, and calibration of the image.

a) Instrumental Signature Removal (ISR)

We begin processing individual exposures by removing the instrumental signatures from DECam and making an initial set of World Coordinate System (WCS) measurements.

In our data repository we have flat, bias, defect, and fringe calibration files. These calibration files are used to enhance the signal-to-noise ratio in the images as much as possible, thereby improving the quality of information we can garner from our images. Removing the instrumental noise includes masking known bad pixels, subtracting the camera's bias, and using flat frames to remove spatial inhomogeneities in the light detection.

 Bias frames are taken with nearly zero exposure time and show the base level of noise contributed by the camera. When photons land on the detector, the number that are counted by the camera is determined by a Gaussian distribution around number of incident photons, because of the readout noise. Some pixels will overcount the number of photons they receive, while
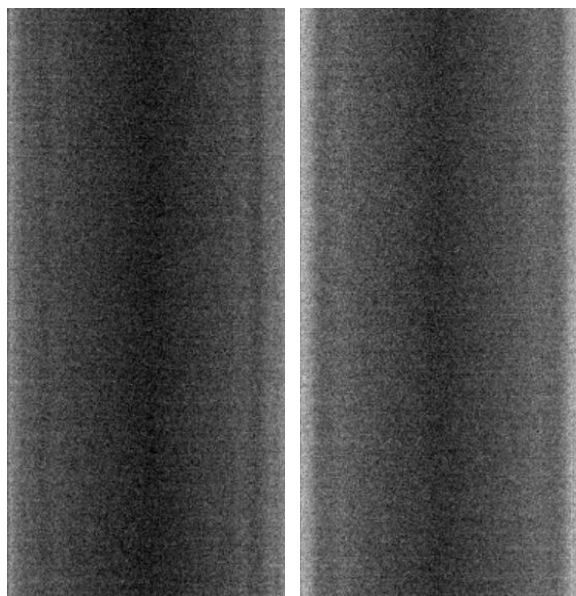
Figure 6: These two images are bias frames used in processing images of A3376. These correspond to two different CCD's.

Left: CCD #25 (S1); Right: CCD #1 (S29)
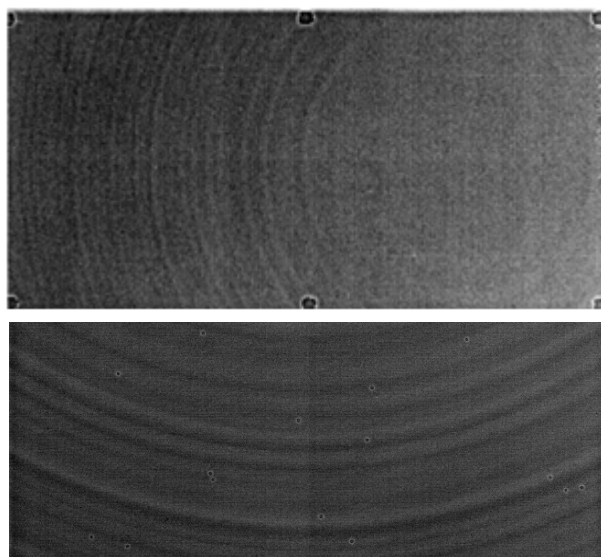
Figure 7: Also used in processing A3376.

Top: This flat frame was taken with and used for calibrating images in the g-band. It corresponds specifically to CCD #25 (S1).

Bottom: This is a zoomed in cut of above image. The donut shapes are created by dust grains on the CCD or the g-band filter.

others will undercount. According to the Gaussian distribution, you would expect some pixels to report receiving a negative number of photons. This of course doesn't happen because a negative photon count isn't physically reasonable. There is therefore a net overcounting of the photons. Generally, the overcounting problem is minimized by applying a bias voltage to the electrical system in the camera. The bias voltage is a constant voltage added to the capacitor before the translation of the signal from analog-to-digital. It creates a reading of a few hundred extra photons even on pixels that receive no light. Though this bias eliminates the problem of negative counts and better preserves the relative photon measurements between pixels, it artificially adds photon readings across the image. These must then be removed in image processing. In order to determine the added light due to the bias voltage, we expose all the CCD's to zero photons by taking a bias frame with zero exposure time. In zero time, there should be no photoelectrons and no thermally excited electrons in the camera system. Figure 6 shows the bias frame from two different CCD chips in used for A3376 processing.

Flat frames are used to remove pixel-by-pixel inconsistencies in signal readout. There are 56 million pixels in DECam, and it is illogical to expect that they might all react to incoming photons identically. The goal of flat frame calibration is to remove the artifacts of inhomogeneous response to photons across the camera. One possible cause of this inconsistency is variable pixel area, because photometric calibration steps will assume that each of the pixels has equal area. However, this isn't much of a concern with DECam images because it introduces an error of less than 1% at the extreme edges. Dust grains on the CCD and filters will also artificially remove light from the image. They appear in the image as dark donuts whose size depends on how far the grain is from the focal plane. These can be seen in Figure 7. We rely on flat frames to correct for the dependence of observed flux on position in the sky. Without calibrating the images using flat frames, we would be unable to carry out photometric analysis.
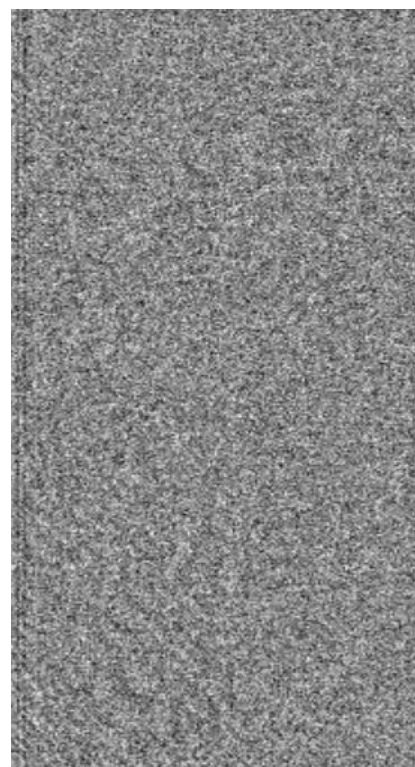
Figure 8: This is a fringe frame used for z-band calibration of CCD #1. (Used in processing A3376)

Further corrections include masking saturated pixels and applying crosstalk corrections. The signals in amplifiers in the instrument can affect the signal picked up by others and this is adjusted for using an empirical crosstalk correction. We also improve image quality in the z and Y bands using fringe frames. The fringe pattern that is added to these images is an interference pattern of the received signal. (See Figure 8)

b) Characterization of the Image

In this step, the important qualities of the calibrated exposure are determined by calling the char image subtask of the LSST Science Pipeline. The image is characterized: the background and Point Spread Function are modelled, cosmic ray signatures (which appear as bright streaks with sharp edges) are removed, bright sources are detected and measured, and an aperture correction is determined.

Accounting for the Point Spread Function (PSF) of the image is absolutely crucial to measurements of a WL signal. Telescopes like DECam introduce a PSF that can be 2-4% intrinsic ellipticity of the galaxies. This is significantly larger than the weak lensing signal which creates a shear of roughly 1% or the intrinsic galaxy ellipticity. Atmospheric seeing also serves to circularize the images of objects, further diluting the lensing signal.

A PSF measurement reads the instrumental response to imaging a point source. Any light source smaller than the maximum resolution of DECam is considered a point source. When such objects are imaged, they appear as extended shapes. The smearing of the point source images is modelled by the PSF. For ground-based optical telescopes, like the one we are using, the majority of the spread is due to atmospheric turbulence (also known as atmospheric seeing). In modelling the PSF, we use the full width at half maximum (FWHM) as a scale width for the PSF. As I will discuss in the coaddition steps, one of the image-quality checks we do concerns the FWHM of objects in the images. If we determine the FWHM of objects in the image are too large, then the smearing of point sources hasn't been reduced adequately by the measured PSF.[13]

---

[13] In 1969, Moffat modeled the PSF of stars in images taken by CCD cameras (such as DECam), His PSF model describes the image flux as function of the distance from the source image's center, $I(r)$, in the following way:

$$I(r) = I_0 \left[1 + \left(\frac{r}{\alpha}\right)^2\right]^{-\beta}$$

Even though the total brightness of an object is not affected by its spread, we must also make an aperture correction. The extension of sources as described by the PSF, the scattering of light in the telescope, and the small size of the pixels all work to diminish the measured magnitude of objects in the image. An aperture correction applies an offset to the image to determine the true magnitude of sources.

c) Calibration of the Image

Finally, external reference catalogs are used for astrometric and photometric calibration of the sources in each image. Astrometry is a reading of the position of a source and photometry measure its brightness in a filter band.

Before running processCcd.py, we set up a configuration file that overrules some of the automatic settings in the LSST Science Pipeline. Most importantly, we request the use of external reference catalogs for astrometry and photometry calibration. We use four separate reference catalogs for calibration: Gaia data release 2, Pan-STARRS1 (PS1) 3pi survey, Sloan Digital Sky Survey (SDSS) Data Release 15, and SkyMapper (SM). The Gaia catalog gives us the highest precision astrometry for any star in the Milky Way and is therefore our first-choice catalog for astrometry calibration. We don't use it for photometry, though, because its set of filters has strongly different wavelength boundaries than the DECam filter set. Pan-STARRS1 (PS1) is our first-choice photometric catalog and second choice astrometric catalog, but it doesn't contain data for regions south of -30 degrees. This isn't generally a problem, but A3376 has a declination of -39.99 degrees and required the use of SkyMapper as the photometric reference catalog. SkyMapper's best quality is that it contains data on objects south of 2 degrees declination. However, SkyMapper is generally not ideal because, according the Shenming Fu's manual, "the u-band has a 1% red leak at 700-750 nm wavelength (however, its v-band performs closer to DECam's u-band)." (Shenming Fu, Ian Dell'Antonio, 2020) In addition to not having

---

where I_0 normalizes the function, β determines the shape of the PSF, and α is some scale factor. Taking into account that the FWHM is by definition the point at which the intensity, $I(r)$, is half of I_0, we find:

$$\alpha = \frac{\text{FWHM}}{2*sqrt(2^{\frac{1}{\beta}}-1)} \quad \text{or} \quad FWHM = 2I_0 * sqrt(2^{\frac{1}{\beta}} - 1)$$

Trujillo et. al found that the Moffat PSF accurately models atmospheric turbulence with β = 4.765.

observations south of 30 degrees, PS1 also doesn't have data in the u-band. This means that we use SDSS for u-band photometry calibration when using PS1 for the other bands.

After the PSF model and aperture correction are applied, an updated source catalog is created. The astrometric calibration step matches sources in the updated catalog and those in the external reference catalog, to fit the DECam image with a better WCS. Ideally, each CCD would have more than 100 matched sources used to precisely calibrate the astrometry. This would give a precision of around 10^{-2} arcseconds. Photometric calibration determines the photometric zero-point, which generally lies around apparent magnitude 30 with an uncertainty of roughly 10^{-4}. The photometric zero-point is the apparent magnitude of a source that creates one count per second. Photometric calibration then uses the equation below to relate the apparent magnitude of an object to the number of counts (or data number), DN, it causes in the observation time EXPTIME:

$$m = -2.5 * log_{10}\left(\frac{DN}{EXPTIME}\right) + ZEROPOINT$$

The photometric zero-point is the missing piece for bridging from an object's count number to descriptions of its incident flux in standard photometric systems.
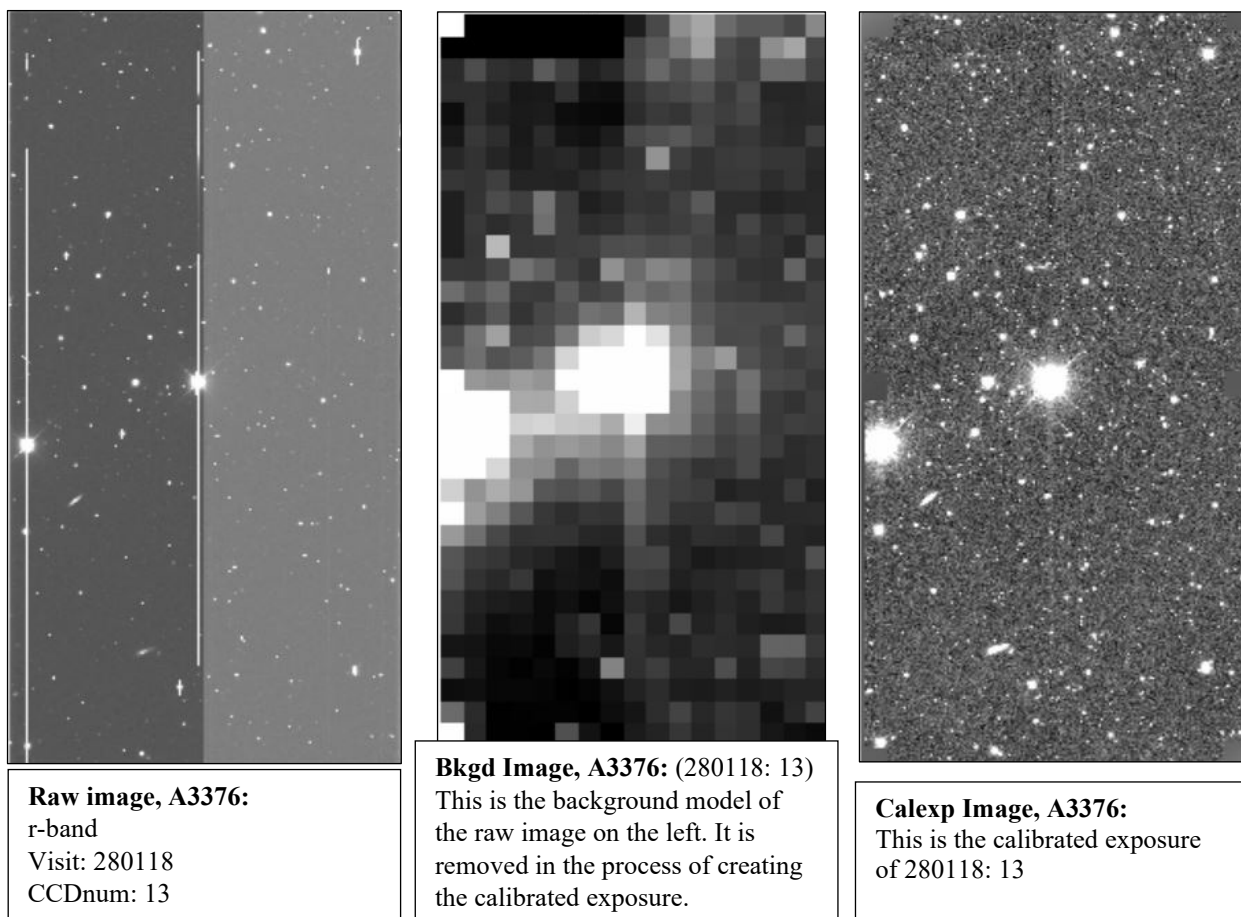
ProcessCcd.py outputs

Once processCcd.py has been applied, the raw DECam image has had its instrumental signatures removed, the PSF and background modeled, an aperture correction applied, and the astrometry and photometry calibrated. We began this process with raw images, master calibration files, and reference catalogs. The output datasets include: calexp, bkgd, Metadata, Src, SrcMatch, icSrc, and postISRCCD.

- Calexp: This folder contains the calibrated images in the form of fits files. The raw image from CCD in each visit has been through the steps outlined above. These are the resulting relatively polished images.

- Bkgd: This folder contains the background models for the calexp calibrated images. These are also stored as fits files.[14]

- Metadata: The files in this folder contain lots of information about the process, including which calibration images and algorithms were used and lists of objects that were rejected. This information is stored in .yaml files.

- Src: In this folder are catalogs of the sources detected in the calibrated images. They contain the photometric and astrometric information of each source, as detected by processCcd.py.

Figure 9: This figure shows the progression of a single raw exposure through this first step of the LSST Science Pipeline.

Raw image, A3376:
r-band
Visit: 280118
CCDnum: 13

Bkgd Image, A3376: (280118: 13) This is the background model of the raw image on the left. It is removed in the process of creating the calibrated exposure.

Calexp Image, A3376:
This is the calibrated exposure of 280118: 13

---

[14] It can be seen in Figure 9 that some of the flux of the bright star is removed when the background is subtracted. Ultimately, this reduces the flux of the star and makes it easier for us measure the nearby objects.

Because it is not part of data set (of background galaxies), we don't care about an artificially low flux measurement for the star.

- SrcMatch: The catalogs in this folder list the matches found between the exposure source catalogs and the external reference catalog. This table is created in the calibration step.

- icSrc: This contains tables of the sources detected after the image is characterized, but before it is calibrated.

- postISRCCD: This simply contains the exposure with the instrumental signature removed.

2) Coadding Single-Exposure Images

Before stacking the individual exposures, we check the image quality of each. Though every visit was processed in the previous step, if the ellipticity or the FWHM of stars in an image is too large, we determine that the image quality of the exposure is still not high enough for us to include it in our final dataset and stacked image. The FWHM is a straight-forward measurement of the image's effective resolution and, as already discussed, is related to the image's PSF. A large FWHM indicates that the seeing in the image is inadequate. We also test the ellipticity, because a large ellipticity indicates smearing in the image. Ideally, the ellipticity of a star should be 0, corresponding to a perfectly circular image. However, between variations of focus across the detector, tracking errors, and atmospheric turbulence, the images of point sources or spherical sources can be elongated.

We work primarily with exposures from 5-filter bands: u, g, r, i, and z.[15] One of these bands is used to measure the weak-gravitational lensing signal and the other four give the color information necessary to determine photometric redshifts. We use either the r or i band for shape measurement and the choice is made based on which band has the longest cumulative exposure time (depth of image) and the best seeing (smallest FWHM and ellipticity). Generally, we use the r-band data because it has more exposure time and because the CTIO+DECam is most sensitive to the r-band. For the shape measuring band, we require the ellipticity of objects in the image to be below 0.13 and the FWHM to be below 4.4 pixels. In the non-shape analysis bands, the requirements are less stringent: e_max=0.33 and fwhm_max=6.6 pixel.

---

[15] When the data is available, we also use images from the Y-band.
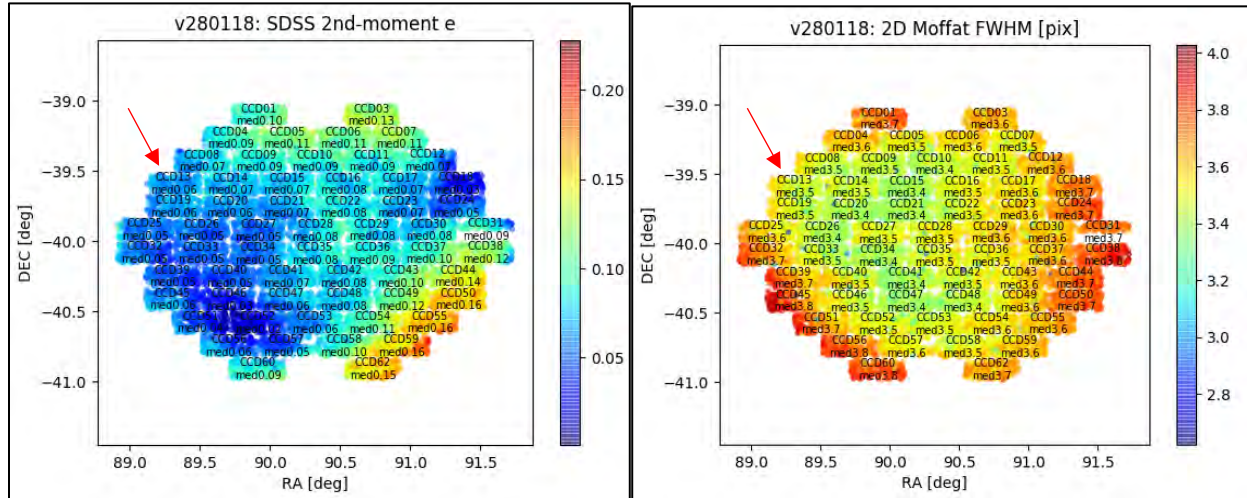
Figure 10: When checking the image quality, we produce these two graphics for each visit. They indicate the image quality, according to our two measures, within the region of sky imaged by each CCD. It can be seen that images taken by the outermost CCDs tend to have the worst quality. These two images, in particular, show the image quality of the visit shown in Figure 9. The properties of the CCD 13 image from visit 280118 are indicated by the red arrows.

We then stack, or coadd, the exposures that pass the image quality checks. Coaddition dramatically increases the signal-to-noise ratio of objects in the image. The first step of this process involves building a *Skymap,* which is used in determining the WCS of the final coadded images. The Skymap is a rendering of the night sky that is divided into rectangles, called tracts. The tracts are overlapping and are, themselves, built of smaller overlapping rectangles, called patches. The tracts, and therefore patches, each have a unique WCS and are warped onto the curved celestial sphere. Because the angular size of the tracts is quite small, they are considered to be flat areas. The WCS of patches within a tract are therefore calculated as changing with flat space geometry. The Skymap we build covers only the finite area of the celestial sphere that contains our processed exposures. The clusters we process have small enough angular size that they each fit within a one tract Skymap, made up of roughly 8x8 patches.

After building the Skymap, we perform *joint calibration*. This step is used to normalize and improve the photometric and astrometric calibrations of all the exposures within a band. Each visit contains calibration information for the same swath of sky. By simultaneously comparing the calibration data for each visit and the reference catalogs, we recalibrate the astrometric and photometric information.

It is worth noting that for a set of exposures from 2014, all with exposure number 21****, the joint calibration process is unable to run. When the process attempts to begin astrometric fitting, the following fatal error is displayed:

"jointcal INFO: Initial chi2/ndof : nan/75692=nan
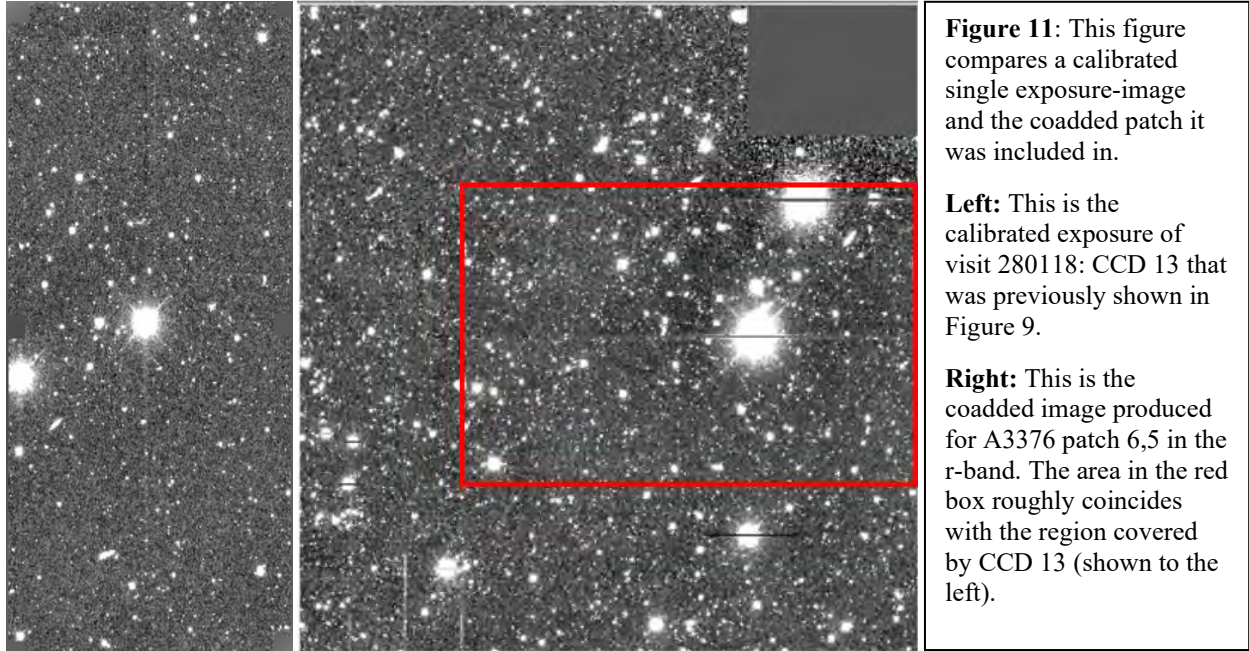jointcal FATAL: Failed processing tract 0, FloatingPointError: ('%s chi2 is invalid: %s', 'Initial', <lsst.jointcal.chi2.Chi2Statistic object at 0x7f6f7198e4c8>)"[16]

This was a significant problem in my attempts to process A2029 data and to build a weak gravitational lensing map of the cluster. I got stuck at this step for quite some time and have struggled to move past it. However, the majority of the other clusters we processed were able to move through this step without problems. A2029 is one of only two clusters that we have stumbled across in our lab with this problem. More observation time on A2029 is scheduled for this upcoming fall, so we are now waiting on that extra data before proceeding with A2029 processing.

Once the astrometry and photometry are simultaneously calibrated for every exposure within a filter band, the next step is to warp the images onto their Skymap patches. Each exposure, with its fresh astrometric and photometric calibrations, is molded onto the appropriate patch of the Skymap built two steps ago. The warped exposures are then stacked on one another creating deep coadded images that span multiple patches. The sources in the coadded images will have increased signal-to-noise ratios and improved shape and flux clarity (see Figure 11). We end this step with a coadded warped image in each filter-band.

Once the coadded and warped image for each patch is created, we create a combined color image (using 3 color bands) of the entire photographed region of our clusters. These images are incredibly massive and detailed. They show the visibly dense centers and the innumerable interesting galaxies. Figure 9 shows the image development from raw image to calibrated image. Figure 11 shows that how that calibrated image is used in the creation of a coadded image. And Figure 12 shows the irg color combined image that coadded image from Figure 11 ends up in.

---

[16] This is a specific failure code pulled from one output file and only an example. The specifics of the error code vary with different data sets.

Figure 11: This figure compares a calibrated single exposure-image and the coadded patch it was included in.

Left: This is the calibrated exposure of visit 280118: CCD 13 that was previously shown in Figure 9.

Right: This is the coadded image produced for A3376 patch 6,5 in the r-band. The area in the red box roughly coincides with the region covered by CCD 13 (shown to the left).

Figure 12: This is the inner section of the irg combined color image of A3376.

3) Multi-band Measurement

Up until this point, the only step that has combined data from the separate bands has been the creation of the color combined images. The goal of this step is to create a thorough multi-band catalog of the sources (stars, galaxies, etc.) in our images.

We begin by building fresh source catalogs from each filter's coadded image. These catalogs will be more thorough because the coadded images are deeper and have higher signal-to-noise ratios than any of the other images we have worked with. Using the python script mergeCoaddDetections.py, we merge the catalogs of sources created for each filter and end up with cohesive tables from each band. Before proceeding, we deblend the sources in the merged coadded catalogs. The goal of deblending is to determine what signal peaks are from the overlapping images of separate objects. Because the overlapping images have different colors, their relative significance across different filters can be used to isolate them. This step involves making sure that the sources detected by each filter are consistent.

The next task involves measuring the shapes and fluxes of sources in the coadded catalogs and determining which band's catalog contains the best photometric information for each source. The preferred filter will vary between objects, because low redshift objects generally appear brighter in the shorter wavelength bands, and vice versa. Some objects also specifically absorb or emit within the wavelength range of particular bands. The preferred position measurement band for each source is referred to as its *reference band*.

Forced photometry defines the position at which we measure a source, across bands, as the location measured in the object's reference band. Each source is then remeasured across all the bands, using the photometry and shape found in its reference band. This allows us to build a consistent multi-band catalog of all the light sources in our image with the best possible photometric information. This forced photometry catalog is output of the LSST Science Pipeline.

4) Analyzing Measurement Results

The forced photometry catalog lists information about all the light sources in our images in a FITS table. To make use of this data, we translate it into CSV and fiat catalogs of all the sources that aren't stars and that were detected with a high enough signal-to-noise ratio.

Fiatmap

In the background section called "Observing Weak Lensing Signals," I discussed how there is an integral mapping from the observed tangential ellipticity of background galaxies to the relative surface density distribution across a cluster. Fiatmap uses this relationship between the shear and the convergence to build projected mass density maps from the fiat source catalogs. On page 25, I explained that Fiatmap creates both an E-mode and a B-mode map of each cluster. The E-mode map shows the mass distribution of the cluster because gravitational lensing produces a curl-free shear on background galaxy images. The B-mode map shows the biases in our measurements that also appear in the E-mode map.

By altering the scale length for weighting the shear-measured galaxies, we can change how smooth or detailed the surface density map is. Each of our cluster images is roughly 30,000 pixels across, so we generally used a scale length of 1000 pixels. Figure 13 shows the E-mode and B-mode maps produced for A3376 using a scale length of 1000 pixels.
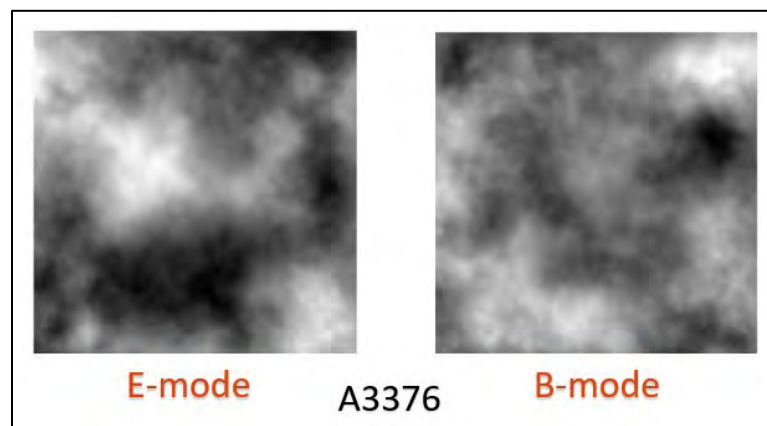
Figure 13: This figure contains the E-mode and B-mode maps produced by Fiatmap for A3376.

Shear Profiles and Mass Fitting

Our final step involves using the data behind the E-mode and B-mode maps to create *shear profile plots* of the tangential and curl ellipticities of the background galaxies as a function of the distance from the center of the cluster. It's worth noting that the cluster center for these plots was

defined by the center of the galaxy distribution, which didn't always perfectly coincide with the WL-defined center.

As I noted before, the projected mass maps we produce only show the relative mass density across the cluster. In order to normalize these maps and determine the total mass of the clusters, we make shear profile mass fits. The total cluster mass is estimated by fitting an NFW profile to the two-dimensional shear profile (called NFW for Navarro, Frenk, and White).[17] Figure 14 shows the shear profile mass fits we created for the clusters in our sample.

To properly fit the cluster mass, we need to know the angular diameter distance to the source, lens, and between the two. In our analysis, however, we assumed that all the shear-measured galaxies where at a redshift of 0.8. In the future, when we calculate the photometric redshift of the shear-measured galaxies, we will be able to vastly improve the accuracy of their reported distances. Measurements of the photometric redshifts will also allow us to remove foreground and cluster galaxies from our shear-measurement sample. Our shear-measurement catalog has requirements for the magnitude and extent of its sources which does a decent, though not thorough, job of excluding foreground and cluster galaxies. The addition of these galaxies to the sample simply dampens the WL signal across the map. This isn't a huge problem when we are looking at comparative substructure, but it does lead to cluster mass underestimates on the order of 2-3. As an example: the mass of A3376 reported by the *Meta-Catalogue of X-ray detected Clusters of galaxies* (MCXC) is larger than our mass measurement by a factor of 2.37.

Contour Overlays

Luckily, comparing the X-ray, DM, and visual substructure isn't reliant on accurate cluster mass measurements. We are able to view and compare the morphology of the clusters from all three signals when we overlay the intensity contours of X-ray and WL signal on the full cluster r-band coadded images. These overlaid images are shown in Figure 15.

---

[17] This essentially entails fitting the NFW shear profile for clusters of different masses to the observed shear profile. The cluster mass is determined by the mass corresponding to the NFW profile that is the best fit.

Results:

This section includes the shear profile mass fits, contour overlay images, and angular alignment data for each of the seven clusters in our sample. All of the results are given in order of ascending cluster mass according to the *Meta-Catalogue of X-ray detected Clusters of galaxies* (MCXC). The masses according to MCXC, as well as other comparative properties of the clusters (X-ray luminosity, radius, redshift) can be found in Appendix B.

This first set of images are the shear profile mass fits for each cluster.
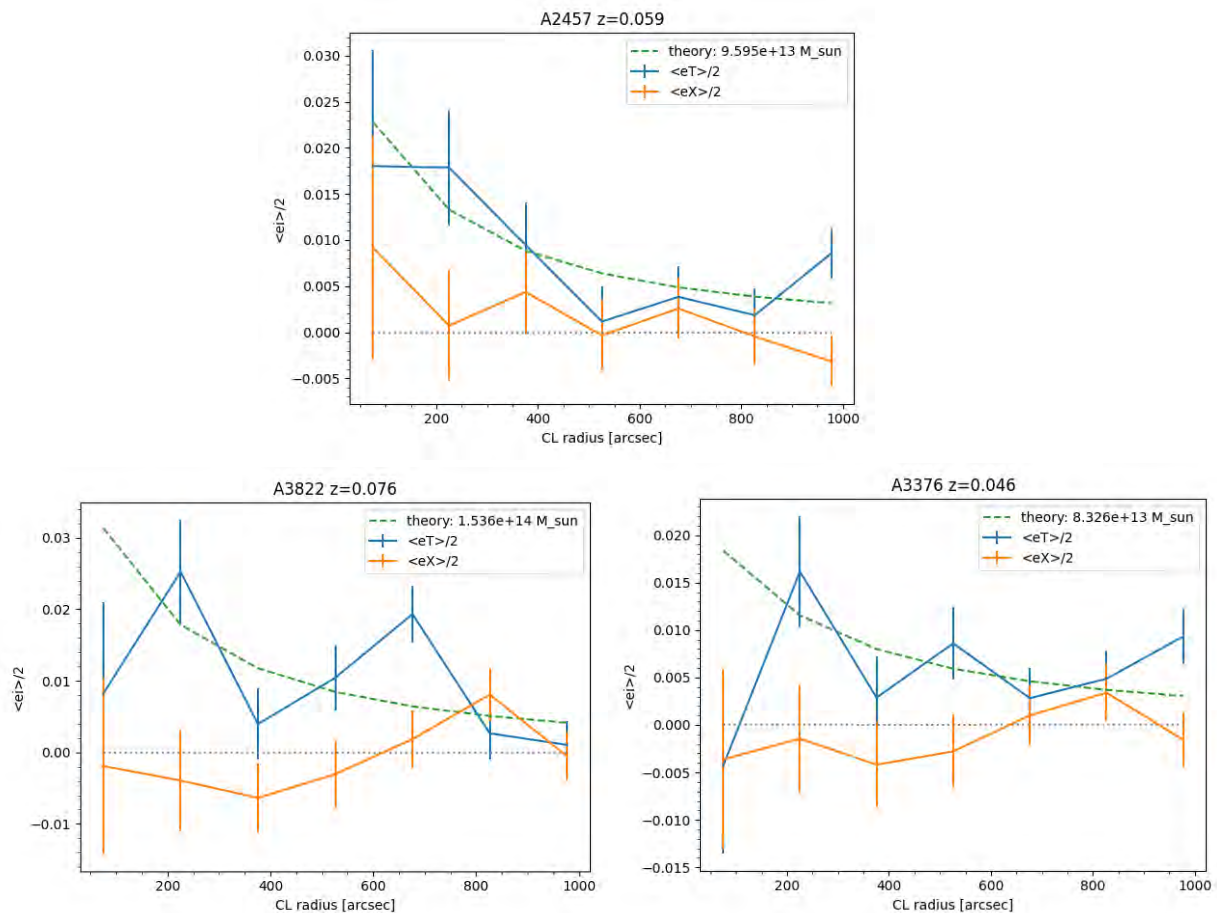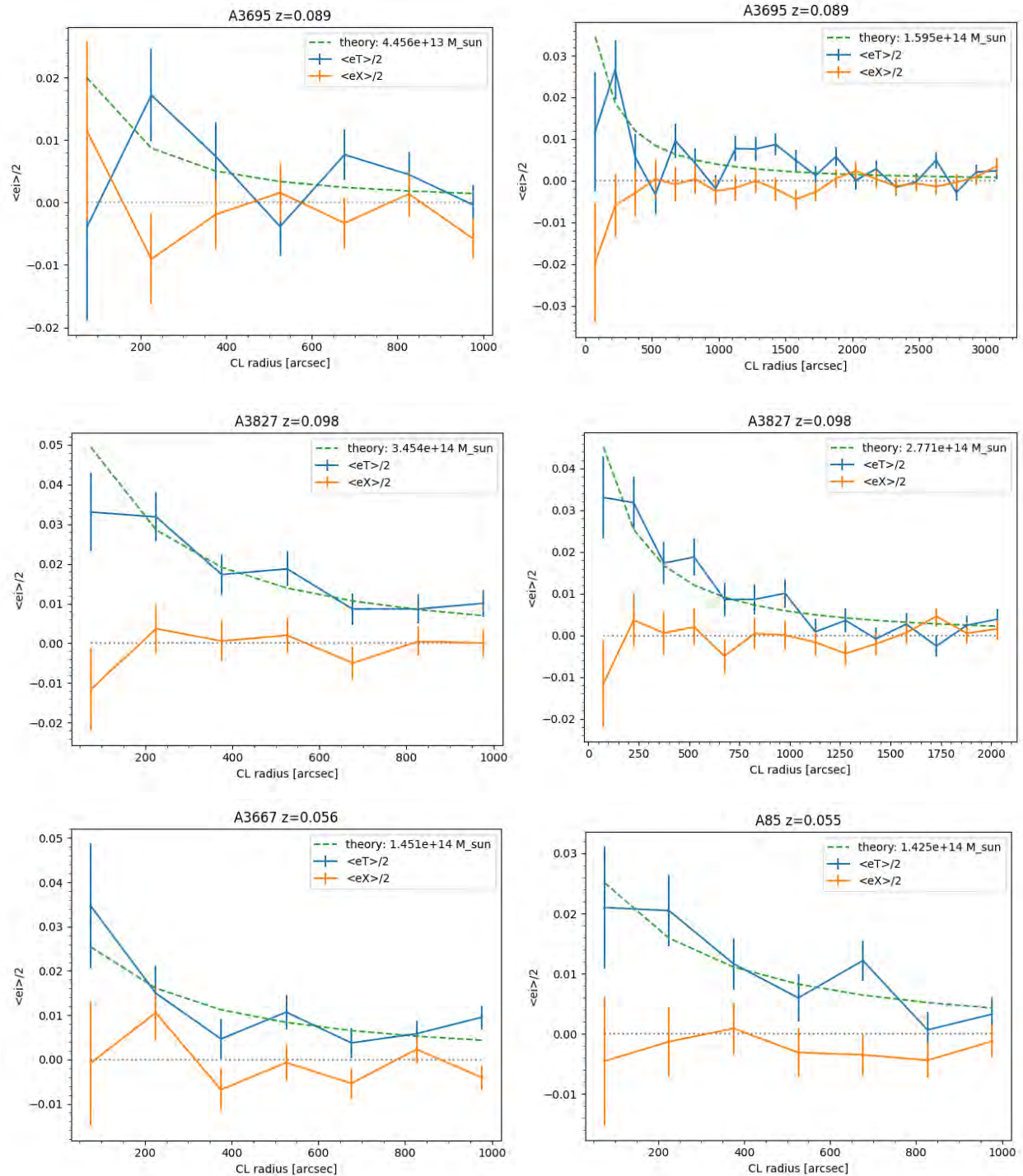
Figure 14: The plots show the shear profile of each of our clusters and the corresponding cluster mass fit. The shear profiles show the tangential and curl-like ellipticities as a function of distance from the cluster center. These profiles are fit with an NFW [Navarro, Frenk, and White] mass profile. Our assumption that all our shear-measured galaxies where at a redshift of 0.8 means that the masses are consistently underestimated by a factor of 2 or 3.
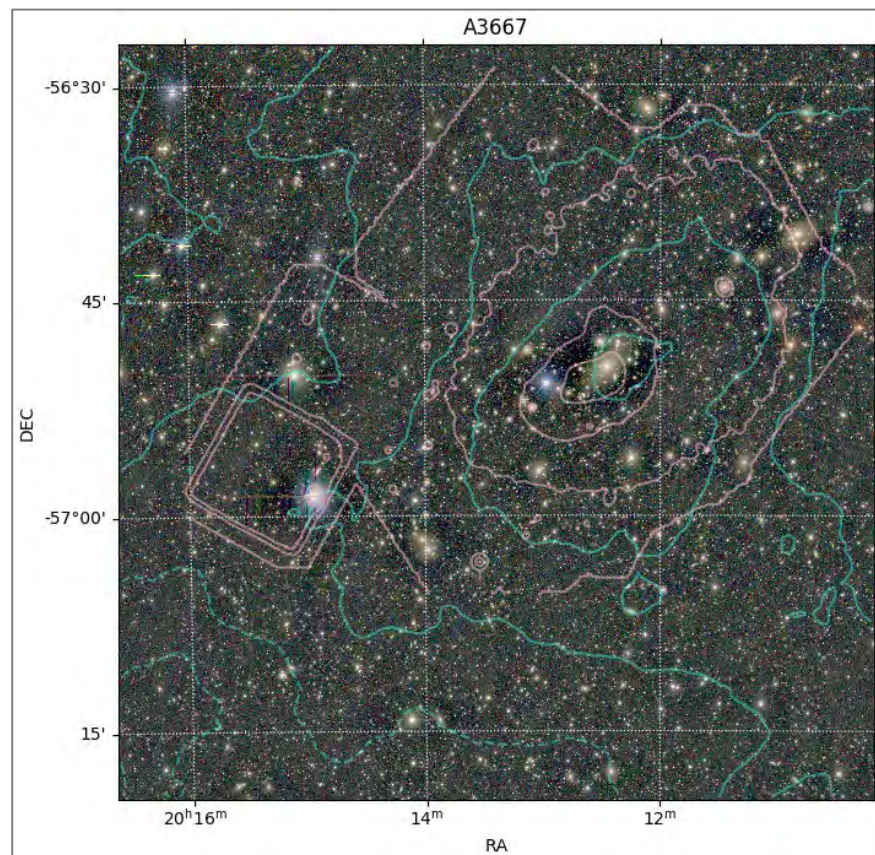
A2457

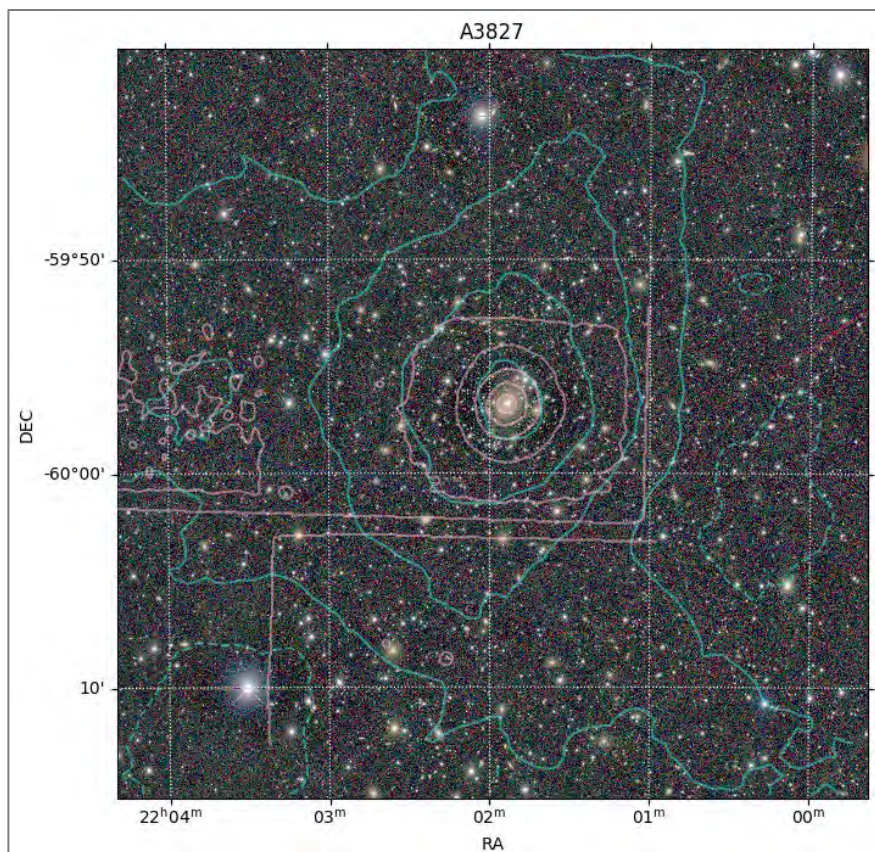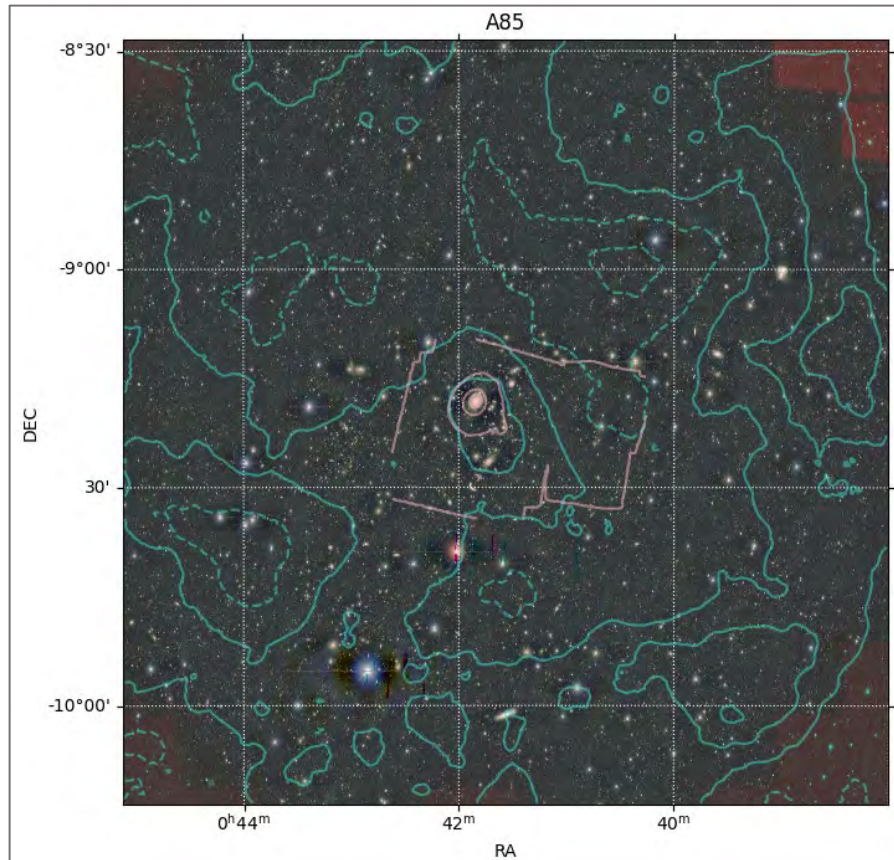A3376

A3822

A3695

A3827

A3667
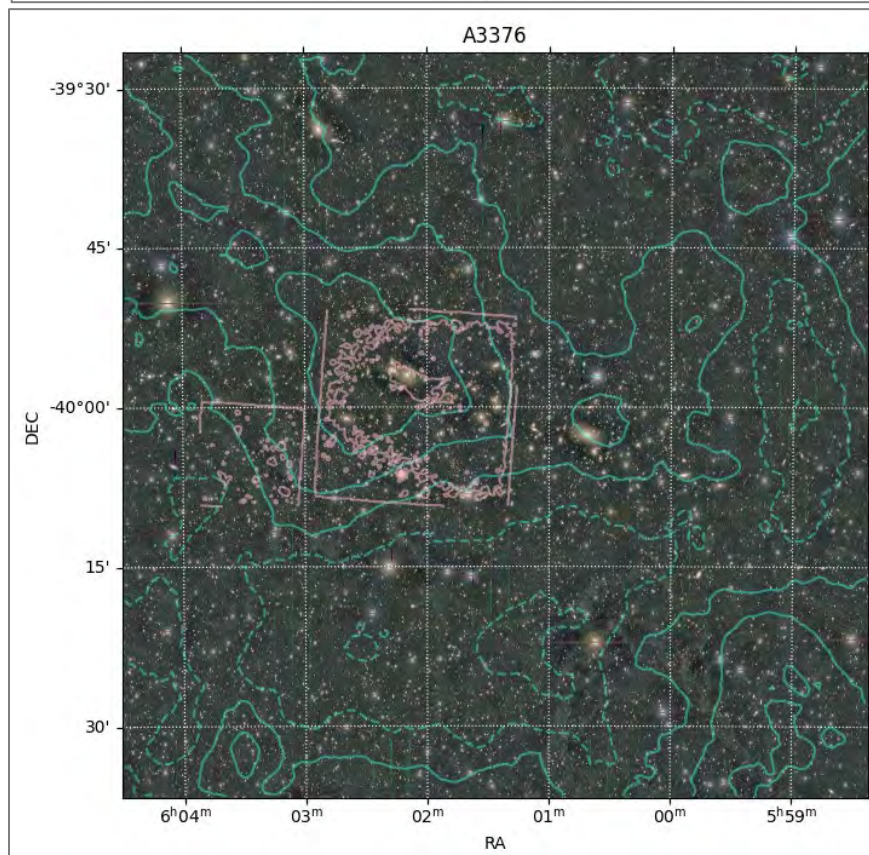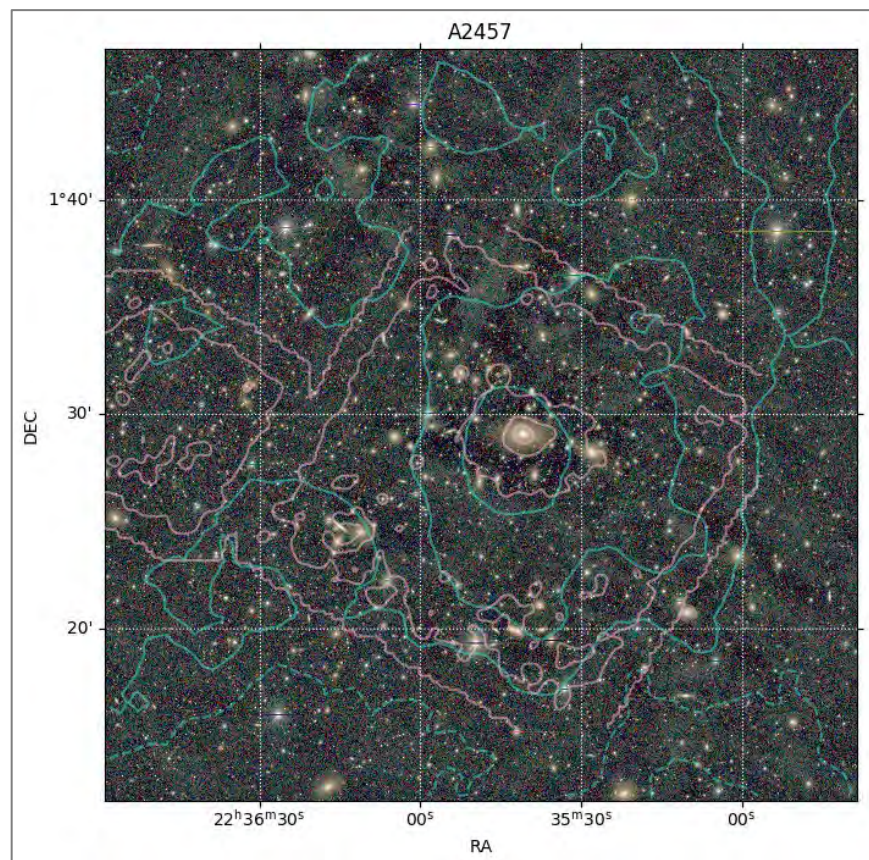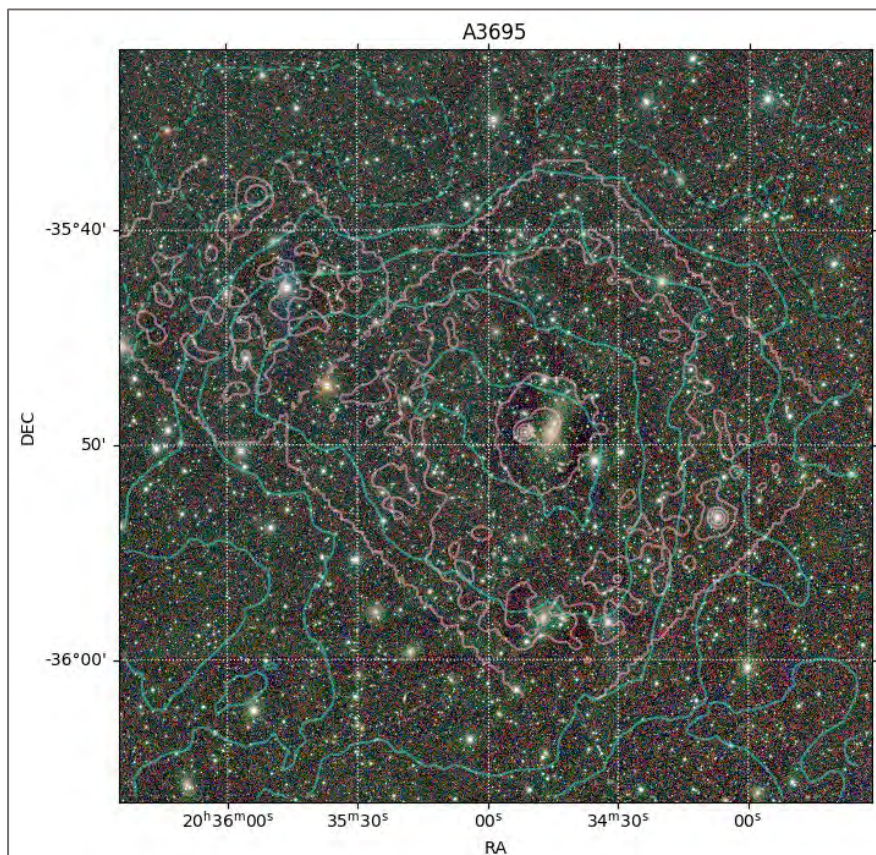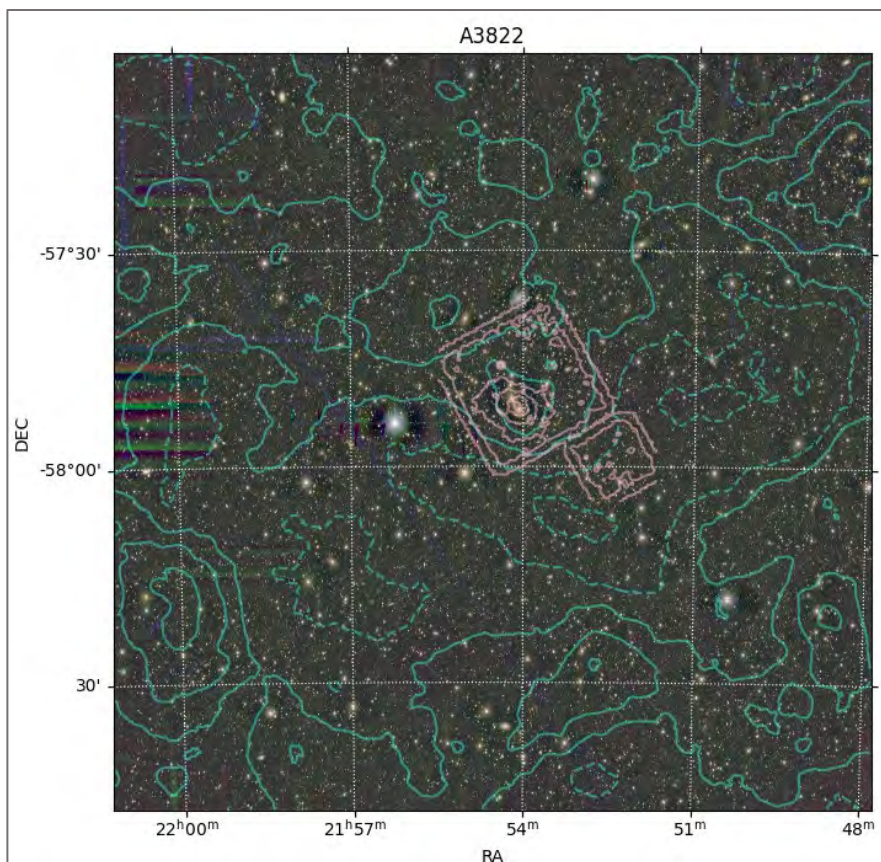
Figure 15: All in all, we found that the peaks of each of the three signals (X-ray, WL, and optical) were nearly overlapping for each cluster. From top to bottom (lowest to highest cluster mass):

A2457: The peaks of the X-ray, WL, and optical signals line-up incredibly well. Both the X-ray gas and dark matter seem to have the same roughly circular density pattern near the cluster core.

A3376: In the cluster center, the three signals' peaks overlap. There does seems to be a second WL peak and corresponding prominent galaxy. However, we don't have X-ray data around the second WL peak to compare with.

A3822: Once again, the optical, X-ray, and WL signals all peak in the same region.

A3695: The peaks coincide, but the X-ray distribution is more circular than that of the DM, which has an elongated contour pattern

A3827: Of this galaxy cluster sample, A3827 has the most circular and perfectly overlapping peaks in all three signals.

A3667: This is the only cluster in which we detect a distinct offset between the X-ray and the WL peaks. However, dark matter substructure seems to overlap well with the BCG. These observations suggest that there may have been a relatively recent subhalo infall into the cluster core.

A85: All three signals peak in the same spot. The X-ray peak is quite round and regular at the cluster center, while the WL peak appears a bit more extended.
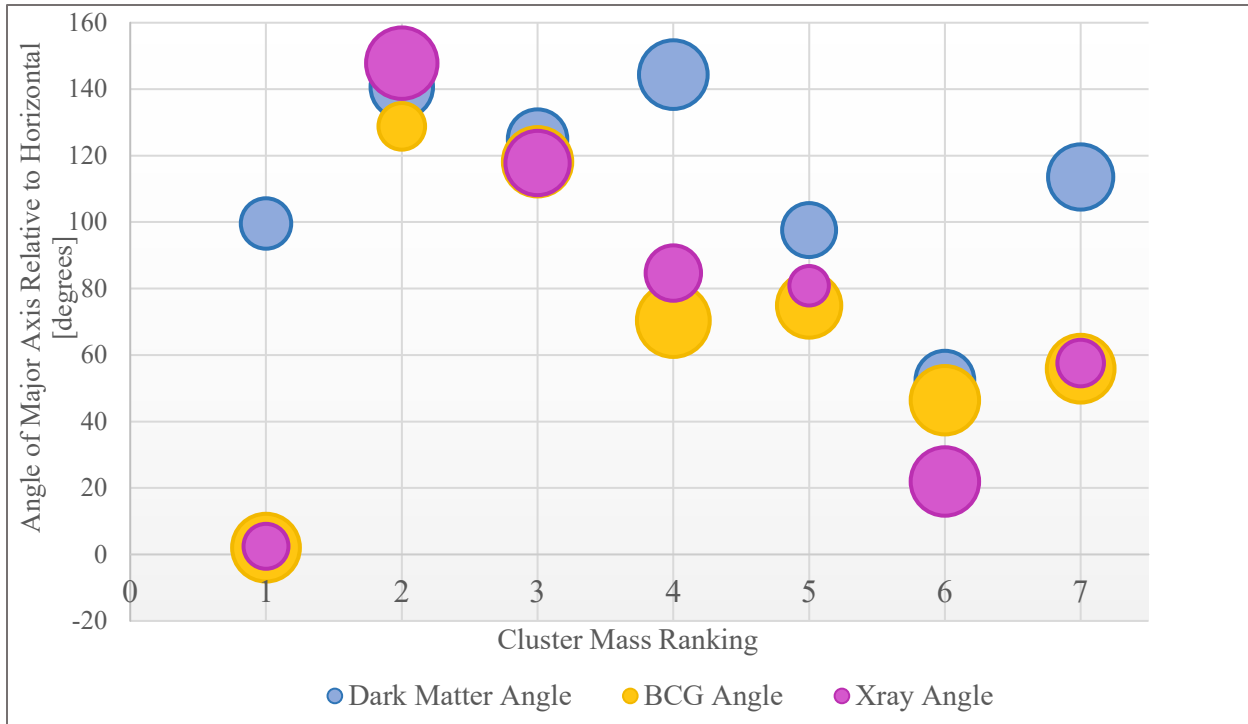
Figure 16: This plot shows the relative angular orientation of the major axis of the WL peak, x-ray peak, and brightest cluster galaxy (BCG). The size of each data point is determined by the ellipticity of the substructure it corresponds to. More elongated structures are denoted by larger circles, whereas small circles indicate that the subhalo appeared nearly circular. We expect the three angles associated with each cluster to be fairly similar. As always, the clusters are given in order of mass (as measured by the MCXC): 1) A2457, 2) A3376, 3) A3822, 4) A3695, 5) A3827, 6) A3667, and 7) A85.

The data displayed in this plot is given in table 2.

We plot the relative angles of the BCG, X-ray emission, and WL-signal peaks, because they can indicate how completely each component has settled into the gravitational potential well of the cluster. We expect the BCG and X-ray gas angles, especially, to coincide, because they are both more likely to trace the cluster's potential well. The dark matter, on the other hand, can maintain the shape and orientation of a subhalo over much longer timescales. Therefore, the alignment of all three signals is an indication of relaxation. By this measure, A3376 and A3822 appear to be the most well relaxed clusters in our sample (see Figure 16). Interestingly, A3667 was the only cluster to show a distinct offset between the X-ray and WL signal peaks in the contour overlay images and is also the only cluster with a poor alignment between the X-ray peak and the BCG. This might be a sign that the X-ray gas in A3667 has recently been disturbed and hasn't had time to settle into the center of the cluster's potential well.

Cluster Name	angle	eccentricity	angle	eccentricity	angle	eccentricity
A2457	2.45	0.560	99.59	0.6278	2.04	0.844
A3376	147.83	0.889	140.64	0.778	128.82	0.580
A3822	117.79	0.801	124.98	0.740	118.16	0.864
A3695	84.67	0.690	144.38	0.855	70.39	0.907
A3827	80.85	0.492	97.61	0.672	74.91	0.801
A3667	21.95	0.852	52.44	0.731	46.41	0.852
A85	57.597	0.58	113.58	0.812	55.90	0.844

Table 2:

This table contains the data displayed above in Figure 16. The pink corresponds to X-ray data, the blue to WL, and the yellow to the BCG. The angles were measured between the X-axis the major axes of the BCG, X-ray, and WL peaks and are given in degrees. The eccentricity measurements show how non-circular each peak. If all three components are roughly circular, differences in their angles are relatively meaningless. However, if they are highly elliptical, the relative angular orientation is more informative. Nearly all of the WL and x-ray measurements were made on the innermost contour

Note: Many of the shapes are not truly elliptical. In my effort to make the eccentricity measurements as accurate as possible, I confirmed that the semi-major and semi-minor axes measurements were nearly perpendicular to one another.

Future Work:

To improve the cluster mass measurements made in this study, our next task is to determine the photometric redshift of the shear-measured galaxies. We would then be able to select solely the background galaxies for shear measurement and to accurately report their redshift, instead of approximating that they all have redshift 0.8.

An interesting question, that I didn't get to dive into, is how the comparative morphologies of these low-redshift clusters behaves as a function of their mass. This analysis will require a much larger sample of clusters. My research is also part of an ongoing project to build a catalogue of projected dark matter density maps for low-redshift galaxies. The future of this project also requires the WL analysis of many more low-redshift galaxy clusters.

Appendix A: Observational Signatures of Ongoing Formation: Coma Cluster

The Coma Cluster ($z = 0.0236$) "has long been considered typical of dynamically relaxed systems. However, a wide range of studies have revealed that it contains complex substructure." (Andrade-Santos, 2013) Simulations predict that the rich Coma cluster has accreted 7 subhalos with mass on the order of $10^{21} \, M_{\odot}$ (Springel et al., 2005; Boylan-Kolchin et al., 2009; Fakhouri et al., 2010; Giocoli et al., 2010). Indeed, observational research of the Coma cluster, in both the optical and X-ray, have detected several accreted subhalos that have yet to be destroyed. Because the Coma Cluster has such a low redshift, it is an ideal candidate for substructure research. Through the Subaru/Suprime-Camera, its large angular size allowed for measurements of subhalos with masses as small as 0.1% the virial mass of the cluster. (Okabe, 2014) Two of the observed subhalos, NGC 4889 and NGC 4874, were found with relative velocities that suggest they have only recently joined the cluster core.

X-ray observations, in particular, have provided evidence of continued infall in the Coma Cluster. In 1997, Vikhlinin et al. found a linear filament reaching roughly 1 Mpc out from the center of the cluster. Andrade-Santos et al (2013) described how it "may be enhanced X-ray emission due to gas stripped from an infalling group or the potential perturbations caused by tidally stripped dark matter." Andrade-Santos et al. (2013) also probed the Coma Cluster's dark matter dominated substructures by examining its X-ray morphology. Subhalos can be responsible for regions of enhanced X-ray emission because they create deeper local pockets in the cluster's gravitational well, thereby attracting and compressing the nearby intracluster medium (ICM). Andrade-Santos analyzed X-ray detected inhomogeneities of the ICM to probe the structure of central subhalos and constrain both their masses and locations in 3-dimensions. He used models of this phenomena to make measurements of the masses of multiple subhalos within the cluster core and to pinpoint their redshifts with a confidence of 90% and no more than $\pm 10 \, kpc$. Andrade-Santos' research on the Coma cluster makes clear how much information can be derived from joint observations of cluster substructure in the X-ray and WL-signal domain:

> Our results highlight the potential for using high quality X-ray data to probe substructure in galaxy clusters. Particularly when used in combination with lensing measurements to constrain the mass of a subhalo, X-ray data can constrain where along our line of sight a subhalo lies within a cluster. The X-ray data can also be used to determine subhalo masses and, potentially, to probe their internal structure, i.e. their truncation and scale radii. (Andrade-Santos et al., 2013)

Appendix B: Comparative Mass Measurement Results from Recent Studies

Earlier in this paper, I discussed three different methods for measuring cluster mass and the degree to which they tend to agree. In this appendix, I am going to elaborate on the specific comparative mass findings of a series of research projects.

As I discussed extensively, A2163 is an irregular cluster with significant WL substructure (Squires, 1997). Squires found that despite the strong indications that A2163 is still undergoing formation his WL and X-ray mass measurements agreed to within 2 sigma error bars. Two simulation studies, using the same measurement methods as Squires, (Schindler, 1996; Eyrard, Metzler, & Navarro, 1996) found that their calculated X-ray masses were in agreement with their cluster model to within $\sim 15 - 20\%$. Schindler (1996) pointed out that "larger deviations can occur, particularly in those cases where a major merger shock wave passes through the cluster – the mass value can be well off, by a factor of 2 locally, near the position of the shock wave – and in cases where major substructural features were not properly accounted for." (Squires et al., 1997)

Wu and Fang (1997) found in their results from a set of 29 clusters that M_{lens} and M_v tend to be in agreements while M_x "systematically underestimated cluster masses by a factor of ~2-3 compared with the gravitational lensing and 'virial' methods, which demonstrates [yet again] that the gas particles may not be a good tracer of the gravitational potential of the cluster." X-ray morphology is traced by the temperature of the ICM and "recent high spectral resolution observations do reveal the occurrence of complex temperature maps, indicating ongoing merger activities in clusters and cluster evolution with cosmic epoch. Overall, the simplification of modeling the temperature (isothermal) and gas density profile (spherical) is responsible for the deficit of the X-ray cluster mass detected in this paper." (Wu & Fang, 1997)

The Weighing the Giants project looked at 51 clusters (von der Linden et al., 2014) and began with the expectation that "even for the most dynamically relaxed clusters, and at optimal radii, hydrostatic X-ray mass estimates are expected to be biased at the 5-10 percent level due to non-thermal pressure support from residual gas bulk motion and other processes (Nagai, Vikhlinin & Kravtsov 2007; Rasia et al. 2012). For less relaxed systems, and for measurements at larger radii, the biases in hydrostatic measurements can be significantly worse (20–30 per cent; Nagai et al. 2007)." (von der Linden et al., 2014)

McCleary (2018) found that for relatively regular clusters, X-ray mass measurements were more accurate. Both A2029 and A1606 have no detected substructure and their mass estimates based on both WL and X-ray signals are in fairly good agreement. On the other hand, A2457 and A85 presented irregularities in the form of substructure and their mass estimates based on WL analysis were found to be 20-30% lower than those determined from X-ray proxies. "These seemingly contradictory findings make sense in a model where X-ray masses rely on an assumption of hydrostatic equilibrium, but only relaxed clusters without major substructure may be assured to be in hydrostatic equilibrium." (McCleary et al., 2018)

Appendix C: Table of Galaxy Cluster Sample's Individual Properties

(1)	(2) z	(3) $L_{x, 500}$	(4) σ_{L_x} [%]	(5) F_x	(6)	(7) M_{500}
A3376	0.047	1.027	4.8	19.70	Chandra	1.97610
A3827	0.098	4.223	6.3	18.20	Chandra	4.58900
A3667	0.056	4.870	5.3	68.00	Chandra	5.16960
A3822	0.076	2.133	6.8	14.90	Chandra	3.04990
A2457	0.059	0.928	15.7	10.70	Chandra	1.81940
A3695	0.089	2.945	12.4	15.40	Chandra	3.72970
A85	0.056	5.006	3.2	71.50	Chandra	5.31630

Table 3: This table contains information reported by the *Meta-Catalogue of X-ray detected Clusters of galaxies* (MCXC), for each cluster considered in this project (Migkas et al., 2020). The X-ray luminosities were calculated using a ΛCDM cosmology with $H_0 = 70\ km\ s^{-1}Mpc^{-1}$, $\Omega_m = 0.3$, and $\Omega_\Lambda = 0.7$. The table columns contain the following information:

(1) Cluster name
(2) Cluster redshift
(3) $L_{x, 500}$: The X-ray luminosity in the energy range 0.1-2.4 keV from within R_{500}. Given in units of $10^{44}erg\ s^{-1}$.
(4) σ_{L_x} [%]: Percentage uncertainty in X-ray luminosity given in (3).
(5) F_x: X-ray flux given in units of $10^{-12}erg\ s^{-1}cm^{-2}$. I have included this to help give a sense of the apparent brightness.
(6) Instrument used in the X-ray analysis.
(7) M_{500}: Total cluster mass out to R_{500}. Given in units of $10^{14}M_\odot$

Note: R_{500} is the standard characteristic radius of the cluster "within which the mean overdensity of the cluster is 500 times the critical density at the cluster redshift." (MCXC - MCXC Meta-Catalog of X-Ray Detected Clusters of Galaxies)

References:

About LSST | Legacy Survey of Space and Time. (n.d.). Retrieved April 9, 2020, from
https://www.lsst.org/about

Andrade-Santos, F., Nulsen, P. E. J., Kraft, R. P., Forman, W. R., Jones, C., Churazov, E., &
Vikhlinin, A. (2013). DARK MATTER SUBHALOS AND THE X-RAY MORPHOLOGY OF
THE COMA CLUSTER. *The Astrophysical Journal*, *766*(2), 107. https://doi.org/10.1088/0004-637X/766/2/107

Applegate, D. E., von der Linden, A., Kelly, P. L., Allen, M. T., Allen, S. W., Burchat, P. R., Burke,
D. L., Ebeling, H., Mantz, A., & Morris, R. G. (2014). Weighing the Giants – III. Methods and
measurements of accurate galaxy cluster weak-lensing masses. *Monthly Notices of the Royal
Astronomical Society*, *439*(1), 48–72. https://doi.org/10.1093/mnras/stt2129

Ay127_GalClusters.pdf. (n.d.). Retrieved April 12, 2020, from
https://www.astro.caltech.edu/~george/ay127/Ay127_GalClusters.pdf

Barbara Ryden. (2017). *Introduction to Cosmology* (2nd ed.). Cambridge University Press.

Bartelmann, M., & Schneider, P. (2001). Weak gravitational lensing. *Physics Reports*, *340*(4), 291–
472. https://doi.org/10.1016/S0370-1573(00)00082-X

Böhringer, H., Soucail, G., Mellier, Y., Ikebe, Y., & Schuecker, P. (1999). *The X-ray Morphology of
the Lensing Galaxy Cluster Cl0024+17*. https://arxiv.org/abs/astro-ph/9910363v1

CCD Image Calibration. (n.d.). AAVSO for Carolyn Hurliss Online Institute for Continuing
Education in Astronomy (CHOICE). https://www.aavso.org/files/image_calibration-v1.pdf

Chapter 2: DECam Imager. (2014). *NOAO Data Handbook*, *2.0.5*.
http://www.ctio.noao.edu/noao/sites/default/files/DECam/DECamUG_v2.0.5-ARW.pdf

Dark Energy Camera (DECam) | CTIO. (n.d.). Retrieved April 9, 2020, from
http://www.ctio.noao.edu/noao/node/1033

Data Management | Legacy Survey of Space and Time. (n.d.). Retrieved April 9, 2020, from
https://www.lsst.org/about/dm

DECam filter information | CTIO. (n.d.). Retrieved April 9, 2020, from
http://www.ctio.noao.edu/noao/content/decam-filter-information

DePoy, D. L., Abbott, T., Annis, J., Antonik, M., Barceló, M., Bernstein, R., Bigelow, B., Brooks, D.,
Buckley-Geer, E., Campa, J., Cardiel, L., Castander, F., Castilla, J., Cease, H., Chappa, S., Dede,
E., Derylo, G., Diehl, H. T., Doel, P., … Zhao, A. (2008). *The Dark Energy Camera (DECam)*
(I. S. McLean & M. M. Casali, Eds.; p. 70140E). https://doi.org/10.1117/12.789466

Donahue, M., Ettori, S., Rasia, E., Sayers, J., Zitrin, A., Meneghetti, M., Voit, G. M., Golwala, S., Czakon, N., Yepes, G., Baldi, A., Koekemoer, A., & Postman, M. (2016). THE MORPHOLOGIES AND ALIGNMENTS OF GAS, MASS, AND THE CENTRAL GALAXIES OF CLASH CLUSTERS OF GALAXIES. *The Astrophysical Journal*, *819*(1), 36. https://doi.org/10.3847/0004-637X/819/1/36

Filippis, E. D., Sereno, M., Bautz, M. W., & Longo, G. (2005). Measuring the Three-dimensional Structure of Galaxy Clusters. I. Application to a Sample of 25 Clusters. *The Astrophysical Journal*, *625*(1), 108–120. https://doi.org/10.1086/429401

Fu, S., Dell'Antonio, I. (2020). *LSST Science Pipelines obs_decam Tutorial*. https://www.overleaf.com/project/5ce6e5cad704814dcc13f184

Getting started with the LSST Science Pipelines—LSST Science Pipelines. (n.d.). Retrieved April 9, 2020, from https://pipelines.lsst.io/getting-started/index.html

Glossary of SDSS Terminology | SDSS. (n.d.). Retrieved April 9, 2020, from https://www.sdss.org/dr12/help/glossary/

Greene, B. (2000). *The elegant universe: Superstrings, hidden dimensions, and the quest for the ultimate theory* (1st Vintage Books ed). Vintage Books.

Instruments by Telescope | CTIO. (n.d.). Retrieved April 9, 2020, from http://www.ctio.noao.edu/noao/content/instruments-telescope

Ivezić, Ž., Kahn, S. M., Tyson, J. A., Abel, B., Acosta, E., Allsman, R., Alonso, D., AlSayyad, Y., Anderson, S. F., Andrew, J., Angel, J. R. P., Angeli, G. Z., Ansari, R., Antilogus, P., Araujo, C., Armstrong, R., Arndt, K. T., Astier, P., Aubourg, É., … Zhan, H. (2019). LSST: From Science Drivers to Reference Design and Anticipated Data Products. *The Astrophysical Journal*, *873*(2), 111. https://doi.org/10.3847/1538-4357/ab042c

Kim, Y.-K. (2012, November 20). *Celebrating the DECam and CTIO's 50th birthday*. https://news.fnal.gov/2012/11/celebrating-the-decam-and-ctio-s-50th-birthday/

Kravtsov, A. V., & Borgani, S. (2012). Formation of Galaxy Clusters. *Annual Review of Astronomy and Astrophysics*, *50*(1), 353–409. https://doi.org/10.1146/annurev-astro-081811-125502

Mantz, A. B., Allen, S. W., Morris, R. G., von der Linden, A., Applegate, D. E., Kelly, P. L., Burke, D. L., Donovan, D., & Ebeling, H. (2016). Weighing the giants– V. Galaxy cluster scaling relations. *Monthly Notices of the Royal Astronomical Society*, *463*(4), 3582–3603. https://doi.org/10.1093/mnras/stw2250

McCleary, J., Dell'Antonio, I., & Huwe, P. (2015). MASS SUBSTRUCTURE IN ABELL 3128. *The Astrophysical Journal*, *805*(1), 40. https://doi.org/10.1088/0004-637X/805/1/40

McCleary, Jacqueline, Dell'Antonio, I., & von der Linden, A. (2018). *Dark Matter Distribution of Four Low-z Clusters of Galaxies*. https://arxiv.org/abs/1812.08356v1

MCXC - MCXC Meta-Catalog of X-Ray Detected Clusters of Galaxies. (n.d.). Retrieved April 13, 2020, from https://heasarc.gsfc.nasa.gov/W3Browse/rosat/mcxc.html

Mellier, Y. (1999). Probing the Universe with Weak Lensing. *Annual Review of Astronomy and Astrophysics*, *37*(1), 127–189. https://doi.org/10.1146/annurev.astro.37.1.127

Meneghetti, M., Rasia, E., Vega, J., Merten, J., Postman, M., Yepes, G., Sembolini, F., Donahue, M., Ettori, S., Umetsu, K., Balestra, I., Bartelmann, M., Benítez, N., Biviano, A., Bouwens, R., Bradley, L., Broadhurst, T., Coe, D., Czakon, N., … Zitrin, A. (2014). THE MUSIC OF CLASH: PREDICTIONS ON THE CONCENTRATION-MASS RELATION. *The Astrophysical Journal*, *797*(1), 34. https://doi.org/10.1088/0004-637X/797/1/34

Migkas, K., Schellenberger, G., Reiprich, T. H., Pacaud, F., Ramos-Ceja, M. E., & Lovisari, L. (2020). Probing cosmic isotropy with a new X-ray galaxy cluster sample through the $L_X - T$ scaling relation. *Astronomy & Astrophysics*, *636*, A15. https://doi.org/10.1051/0004-6361/201936602

Mulchaey, J. S. (2000). X-Ray Properties of Groups of Galaxies. *Annual Review of Astronomy and Astrophysics*, *38*(1), 289–335. https://doi.org/10.1146/annurev.astro.38.1.289

Narayan, R., & Bartelmann, M. (1996). *Lectures on Gravitational Lensing*. https://arxiv.org/abs/astro-ph/9606001v2

Neilson, Jr., E. (2010). *PSFs and Sampling of Images in Astronomy*. http://web.ipac.caltech.edu/staff/fmasci/home/astro_refs/PSFsAndSampling.pdf

NOAO Science Archive: Search NOAO data. (n.d.). Retrieved April 9, 2020, from http://archive1.dm.noao.edu/search/query/

Okabe, N., Futamase, T., Kajisawa, M., & Kuroshima, R. (2014). SUBARU WEAK-LENSING SURVEY OF DARK MATTER SUBHALOS IN THE COMA CLUSTER: SUBHALO MASS FUNCTION AND STATISTICAL PROPERTIES. *The Astrophysical Journal*, *784*(2), 90. https://doi.org/10.1088/0004-637X/784/2/90

Photometric Zero Point. (n.d.). Retrieved April 9, 2020, from http://www.stsci.edu/documents/dhb/web/c32_wfpc2dataanal.fm1.html

Piffaretti, R., Arnaud, M., Pratt, G. W., Pointecouteau, E., & Melin, J.-B. (2011). The MCXC: A Meta-Catalogue of X-ray detected Clusters of galaxies. *Astronomy & Astrophysics*, *534*, A109. https://doi.org/10.1051/0004-6361/201015377

Readout Noise, and Total Noise. (n.d.). Retrieved April 9, 2020, from http://spiff.rit.edu/classes/phys445/lectures/readout/readout.html

Refregier, A. (2003). Weak Gravitational Lensing by Large-Scale Structure. *Annual Review of Astronomy and Astrophysics*, *41*(1), 645–668. https://doi.org/10.1146/annurev.astro.41.111302.102207

Sagan, C. (2013). *Cosmos* (Ballantine Books Trade Paperbacks, 2013). Ballantine.

Schneider, P. (2006). *Extragalactic Astronomy and Cosmology an Introduction*. Springer-Verlag.

Squires, G., Neumann, D. M., Kaiser, N., Arnaud, M., Babul, A., Böhringer, H., Fahlman, G., & Woods, D. (1997). Weak Gravitational Lensing and X-Ray Analysis of Abell 2163. *The Astrophysical Journal*, *482*(2), 648. https://doi.org/10.1086/304160

Staff, P. A. (2018, June 28). A Brief Guide to Calibration Frames: Bias, Dark, Flats and Dark Flats. *Practical Astrophotography Magazine*. https://practicalastrophotography.com/a-brief-guide-to-calibration-frames/

The Large Synoptic Survey Telescope | Rubin Observatory. (n.d.). Retrieved May 12, 2020, from https://www.lsst.org/lsst/

Vikhlinin, A., Kravtsov, A. V., Burenin, R. A., Ebeling, H., Forman, W. R., Hornstrup, A., Jones, C., Murray, S. S., Nagai, D., Quintana, H., & Voevodkin, A. (2009). CHANDRACLUSTER COSMOLOGY PROJECT III: COSMOLOGICAL PARAMETER CONSTRAINTS. *The Astrophysical Journal*, *692*(2), 1060–1074. https://doi.org/10.1088/0004-637X/692/2/1060

von der Linden, A., Allen, M. T., Applegate, D. E., Kelly, P. L., Allen, S. W., Ebeling, H., Burchat, P. R., Burke, D. L., Donovan, D., Morris, R. G., Blandford, R., Erben, T., & Mantz, A. (2014). Weighing the Giants – I. Weak-lensing masses for 51 massive galaxy clusters: Project overview, data analysis methods and cluster images. *Monthly Notices of the Royal Astronomical Society*, *439*(1), 2–27. https://doi.org/10.1093/mnras/stt1945

Watt, M. P., Ponman, T. J., Bertram, D., Eyles, C. J., Skinner, G. K., & Willmore, A. P. (1992). The morphology and dark matter distribution of the Coma cluster of galaxies from X-ray observations. *Monthly Notices of the Royal Astronomical Society*, *258*, 738–748. https://doi.org/10.1093/mnras/258.4.738

Welcome | Legacy Survey of Space and Time. (n.d.). Retrieved April 9, 2020, from https://www.lsst.org/

Wu, X.-P., & Fang, L.-Z. (1997). A Statistical Comparison of Cluster Mass Estimates from Optical/X-Ray Observations and Gravitational Lensing. *The Astrophysical Journal*, *483*(1), 62–67. https://doi.org/10.1086/304235